Experimental study of uni- and bi-directional exchange flows in a large-scale rotating trapezoidal channel

Maria Chiara de Falco, Claudia Adduce, Alan Cuthbertson, Janek Laanearu, Daniela Malcangio, Joël Sommeria, Maria-Eletta Negretti

Experimental study of uni and bi-directional exchange flows in a large scale rotating trapezoidal channel

Maria Chiara De Falco,[1] Claudia Adduce,[1, a)] Alan Cuthbertson,[2] Maria Eletta Negretti,[3] Janek Laanearu,[4] Daniela Malcangio,[5] and Joel Sommeria[3]

[1)]*Department of Engineering, University Roma Tre, Via Vito Volterra 62, 00148 Rome, Italy*

[2)]*School of Science and Engineering, University of Dundee, Dundee, DD1 4HN, UK.*

[3)]*LEGI, UGA/CNRS, UMR5519, 1209-1211 Rue de la Piscine Domaine Universitaire, 38400 Saint Martin d'Hères, France.*

[4)]*Department of Civil Engineering and Architecture, Tallinn University of Technology, Ehitajate tee 5, 19086 Tallinn, Estonia.*

[5)]*Department of Civil, Environmental, Land, Building Engineering and Chemistry (DICATECh), Polytechnic University of Bari, Via Edoardo Orabona 4, 70125 Bari, Italy.*

(Dated: 9 January 2021)

A large-scale experimental study has been conducted at the Coriolis Rotating Platform to investigate the dynamics of uni and bi-directional exchange flows along a channel with a trapezoidal cross-section under the influence of background rotation. High-resolution two-dimensional Particle Image Velocimetry and micro-conductivity probes were used to obtain detailed velocity fields and density profiles of the exchange flow generated across the channel under different parametric conditions. Experimental measurements give new insight into the stratified-flow dynamics dependence on the magnitude of Burger number, defined as the ratio of the Rossby radius to the channel width, such that values lower than 0.5 characterize unsteady exchange flows. The measurements highlight the role that both ambient rotation and net-barotropic forcing have on the geostrophic adjustment of the dense outflowing layer and on the corresponding counter-flowing water layer fluxes. The coupled effect of these two parametric conditions largely affects the transverse velocity distribution and, for the largest net-barotropic flow in the upper fresh water layer, leads to the partial blockage of the lower saline outflow. Moreover, an increase in the mixing layer thickness, associated with larger rotation rates, and due the interface dynamics, is observed, with shear-driven interfacial instabilities analysed to highlight the influence of both ambient rotation and net-barotropic forcing.

[a)]Electronic mail: claudia.adduce@uniroma3.it.

I. INTRODUCTION

Uni and bi-directional exchange flows are initiated when horizontal density differences and/or pressure gradients develop between adjacent connected volumes containing different fluids. These flows occur in natural aquatic environments, for example, for salt and fresh water exchange between estuaries, fjords or lagoons and coastal seas; and within submarine channels connecting deep ocean water basins with different densities (i.e. through variations in salinity and temperature). Similarly, exchange flows can develop within the atmosphere in the form of sea breezes in coastal regions or thermal winds that can be topographically constrained through valleys or over mountain ridges. In both aquatic and atmospheric domains, these exchange flows can play a key role in the pollutants advection, affecting both air and water quality and having significant environmental health impacts (Filleul et al., 2006; Lu and Turco, 1994; Simpson, 1994). Moreover, the dynamics of the exchange flow generated by temperature differences, between an interior space and the external ambient, has raised much recent attention given the role of building ventilation on the possible pathways of airborne particle and diseases, such as COVID 19 (Dalziel and Lane-Serff, 1991; Linden, 1999; Mingotti et al., 2020; Bhagat et al., 2020). As for natural ventilation, investigation of the interaction between two water masses, with different water proprieties, due to density differences or the presence of particles in suspension, is necessary to understand the driving mechanism of circulation within estuaries and fjords and exchange flow through sea straits (MacCready et al., 2020). Here, mixing occurs across the interface between the two counter-flowing layers and determines the final water properties transported and distributed by the flow (Gregg et al., 2018; Caulfield, 2020; Balasubramanian and Zhong, 2018). At larger scale, when the dimensions of the exchange flow (and notably width) are larger than the Rossby deformation scale, the dynamics are affected by the Coriolis force due to the rotation of the Earth. In fact, the Rossby radius of deformation represents the length scale at which the Coriolis force becomes comparable to the horizontal pressure gradient term and thus rotational effects cannot be neglected, since they deeply affect the evolution of the flow (e.g., Gill, 1982).

The present study focuses on the dynamics of the exchange flows between adjacent water bodies and the relation to a set of external driving parametric conditions. The dynamics of these buoyancy-driven flows are controlled by (i) topographic constraints imposed by seafloor bathymetry, channel shape and roughness, (ii) external forcing due to tides, freshwater inflows, wind-driven surface currents, and (iii) Coriolis forces due to the Earth's rotation. These combined

effects can exert significant influence on the density and velocity distributions, as well as on the diapycnal mixing and secondary circulations generated near rigid boundaries and the interface (Andrejev et al., 2004; Cuthbertson et al., 2014; Dai and Wu, 2016, 2018; Inghilesi et al., 2018; Johnson and Ohlsen, 1994; Kóuts and Omstedt, 1993; Laanearu et al., 2014; La Rocca et al., 2013; Lombardi et al., 2018; Martin and Lane-Serff, 2005; Martin et al., 2005). In particular, shear-induced interfacial mixing within stratified exchange flows commonly results in fluid entrainment/detrainment between the counterflowing fluid layers (Cenedese et al., 2004; Cenedese and Adduce, 2008, 2010; Ottolenghi et al., 2016, 2017). This depends primarily on the buoyancy flux in the lower saline layer and the relative forcing of the upper freshwater layer, which can result in strong vertical gradients in the resulting velocity and density fields, and, consequently, high gradient Richardson numbers (Laanearu et al., 2014; Sargent and Jirka, 1987), while other regions with more restricted exchange (e.g. over fjordic sills) often lead to the formation of interfacial waves along the density interface, transforming into interfacial instabilities (e.g. Kelvin–Helmholtz or Holmboe instabilities) that provide additional local mechanisms for vertical mixing (Fouli and Zhu, 2011; Lefauve and Linden, 2020; Negretti et al., 2007, 2008).

Understanding of these stratified flow processes is thus particularly relevant in coastal regions, where water mass and nutrient exchanges between both tidal and non-tidal inlets (e.g. estuaries, lagoons, fjords, sea straits) and open marine waters can be strongly regulated by channel topography and bathymetric features such as submerged sills, sand bars or confined passages. These features have significant implications for the intrusion of saline marine waters and flushing of semi-enclosed estuarine impoundments, fjords and regional seas (De Falco et al., 2021, 2020; Farmer and Armi, 1999; La Forgia et al., 2020; Matthäus and Ulrich Lass, 1995; Ottolenghi et al., 2020; Wu and Dai, 2020). Indeed, a recent study by Cuthbertson et al. (2018) demonstrated the intrusion and blockage of dense saline water across a submerged sill to be primarily controlled by the volume flux ratio between the barotropically-forced upper freshwater layer and the buoyancy-dominated lower saline intrusion layer within the stratified exchange flow, along with the sill submergence depth itself.

Earth rotation effects also introduce geostrophic adjustment of these long-term internal fluid motions (Cuthbertson et al., 2011, 2014) that can suppress turbulent mixing generated at the interface (Maxworthy, 1986) and result in the development of Ekman boundary layers that induce secondary, cross-channel circulations (Davies et al., 2006; Cossu and Wells, 2010, 2013; Johnson and Ohlsen, 1994; Wells and Cossu, 2013). However, the transverse secondary circulation in

dense water outflows, induced by increasing rotation rates, is also observed to cause higher entrainment velocities along the lateral edges of the intrusions, leading to an overall increased mixing (Arneborg et al., 2007; Berntsen et al., 2016; Darelius, 2008; Fer et al., 2010; Umlauf et al., 2010). Recent numerical studies by Cuthbertson et al. (2020) considered the effect of rotation on saline intrusion across a rectangular submerged sill. These simulations indicated that Coriolis forces can provide an additional blockage mechanism to the saline intrusion, compared to equivalent non-rotating sill exchange flow conditions (Cuthbertson et al., 2018). This blockage was particularly evident when the Rossby number associated with the saline intrusion layer was considerably lower than unity. The Rossby number, Ro represents the ratio of inertial to Coriolis forces, which means that for smaller values of this non-dimensional number, the flow is largely affected by Earth rotation. The finding in (Cuthbertson et al., 2018) was largely attributed to Ekman dynamics and the development of strong secondary circulations in the rotating exchange flows, and within the lower saline intrusion layer in particular. These circulations were found to control the lateral distribution and extent of the lower saline intrusion across the sill and, hence, defined the parametric conditions under which full saline intrusion blockage occurred. In a similar study of rotating uni-directional exchange flows, i.e. gravity currents, along a straight, rectangular channel, Cossu and Wells (2010) found that the gravity current structure and propagation characteristics were also largely unaffected by Coriolis forces under higher Rossby numbers [i.e. $Ro \gg O(1)$]. In this case, it is expected that the inertial and centrifugal forces only dominate in the dynamics of uni-directional stratified flow. By contrast, when gravity current scales were much larger than the Rossby radius of deformation (i.e. $Ro \ll 1$), the Coriolis effects cannot be neglected as they have a profound influence on the flow dynamics (Cossu et al., 2010; Davarpanah Jazi et al., 2020; Griffiths, 1986). The influence of rotation on the magnitude and stability of lock-exchange flows generated in a horizontal rectangular channel with a width constraint but no depth changes (e.g. narrows or straits in shallow seas) has also been investigated experimentally (Rabe et al., 2007). In the latter mentioned study, they concluded that the exchange flow fluxes through the channel were dependent on the magnitude of the Burger number Bu defined by the ratio of the Rossby radius of deformation R and the channel width W at the narrows [note: Bu is also represented by the ratio of Rossby and Froude numbers squared and expresses an indication of the effects of stratification and Earth's rotation (Cushman-Roisin and Beckers, 2011)]. Specifically, for $Bu > 1$ (and, hence, $W < R$), the exchange fluxes were mainly affected by the channel width (similar to non-rotating exchange flows), while for $Bu < 1$ (and, hence, $W > R$), the fluxes were limited

solely by the Rossby radius. The study by Rabe et al. (2007) also highlighted that the rotating lock-exchange flows for very small Burger numbers ($Bu < 0.5$) did not reach a steady state condition (i.e. geostrophic adjustment), but were instead characterized by an unsteady, meandering current and several eddies or gyres forming in the width-constrained channel. This type of S-shape meander in dense rotating fluid layers, beneath a stagnant lower density fluid layer, was also shown to form in a gradual depth-varying, silled channel as a result of flow separation and reattachment of the flow upstream of the sill, leading to the development of a closed gyre at the channel inlet (Borenäs and Whitehead, 1998). Their theoretical considerations of the hydraulically-controlled, constant potential vorticity flows also demonstrated this gyre development under specific experimental conditions.

In practical terms, field observations in the Baltic Sea have also demonstrated that exchange flows through a number of sea straits (e.g. Irbe and Bornholm) reveal a similar meandering (or S-shape) flow patterns in the lower dense water layer (Laanearu et al., 2000; Liljebladh and Stigebrandt, 1996; Lilover et al., 1998). For example, within the Irbe Strait, the Rossby radius of deformation R is estimated to be 2.8 km, based on a bottom dense water layer thickness of 10 m (Laanearu et al., 2000) and taking account of the local Coriolis parameter 7.73 x $10^{-4}\mathrm{rad}\cdot\mathrm{s}^{-1}$ and reduced gravity $1.2\mathrm{x}10^{-2}\mathrm{m}\cdot\mathrm{s}^{-2}$ (Laanearu and Lundberg, 2003), while the interfacial width W through the strait was estimated to be 10 km (Lilover et al., 1998). Similarly, from observations in the Bornholm Strait, (Liljebladh and Stigebrandt, 1996) estimated the Rossby radius based on the interfacial height to be $R = 8$ km, for local Coriolis parameter 7.48 x $10^{-4}\mathrm{rad}\cdot\mathrm{s}^{-1}$ and reduced gravity 8.2 x $10^{-2}\mathrm{m}\cdot\mathrm{s}^{-2}$ (Laanearu and Lundberg, 2003), with an interfacial width W between 25-30 km. As such, the Burger numbers $Bu = R/W$ for the dense water flows through both straits appears to be between 0.28 (Irbe) and 0.32 (Bornholm), which is in general accord with the $Bu < 0.5$ condition for meandering currents found by Rabe et al. (2007) (Note: their Rossby radius was based on the full depth of the lock-exchange flow rather than the interfacial height). In sea straits, however, the fluid dynamics of the dense layer can also be influenced strongly by the upper layer flow, within which the dynamics may be not buoyancy-driven (e.g. in the Baltic Sea, where wind forcing and/or freshwater inputs have a strong effect on sea-level changes and, hence, net barotropic forcing). For this reason, one of the key aims of the current study will be to determine the effects of net barotropic forcing in the upper layer on rotating exchange flow dynamics and fluxes.

Furthermore, many of these previous experimental studies have been conducted in rectangular

channels with horizontal (width) or vertical (depth) constraints imposed. However, clearly the majority of silled channels and/or sea straits will have more natural quadratic-shaped topographies, with non-uniform lateral variations in depth, and, as such, the potential contribution of the side-slopes to the dynamics of exchange flows generated through non-rectangular channels remains largely unresolved. Recent experimental studies of dense uni-directional exchange flows generated in rotating (Cuthbertson et al., 2011, 2014; Darelius, 2008) and non-rotating (Laanearu et al., 2014) flow systems have indicated that a rigid, V-shaped channel topography has a strong influence on both the transverse flow distribution and associated interfacial mixing characteristics along and across the channel.

The overall aim of the present work is therefore to investigate both rotating and non-rotating uni and bi-directional exchange flows along a trapezoidal-shaped channel to determine the relative influence of net-barotropic upper layer forcing and Coriolis accelerations on the lateral distribution of the counter-flowing water masses, interfacial mixing characteristics and the generation of secondary flow circulations. It will also investigate the range of parametric conditions under which stable geostrophic adjustment in the exchange flow is achieved and the conditions under which unstable (e.g. meandering) bottom layer outflows are observed.

The paper is structured as follows. Details of the flow system and experimental apparatus are given in Part II. Part III then presents experimental measurements outlining the dynamics of the uni and bi-directional exchange flows through the analysis of two-dimensional (2D) velocity fields obtained by particle image velocimetry. The analysis of density profiles and mixing layer thickness is then discussed in Part III B, while the geostrophic adjustment of the dense outflowing layer under different net-barotropic conditions and background rotation is presented in Part III C. Part III D presents the evolution of the shear and density layers thickness and the interfacial instabilities, while the along-channel fresh and saline mass fluxes through the trapezoidal channel is discussed in Part III E. Finally conclusions are drawn in Part IV.

II. FLOW SYSTEM AND EXPERIMENTAL APPARATUS

Large scale laboratory experiments were conducted in the Coriolis Rotating Platform at the Laboratoire des Écoulements Géophysiques et Industriels (LEGI) in Grenoble. This facility consists of a 13 m diameter and 1.2 m deep circular tank that can be rotated in a anti-clockwise direction at a constant angular velocity Ω to simulate the Coriolis force experienced in the North-

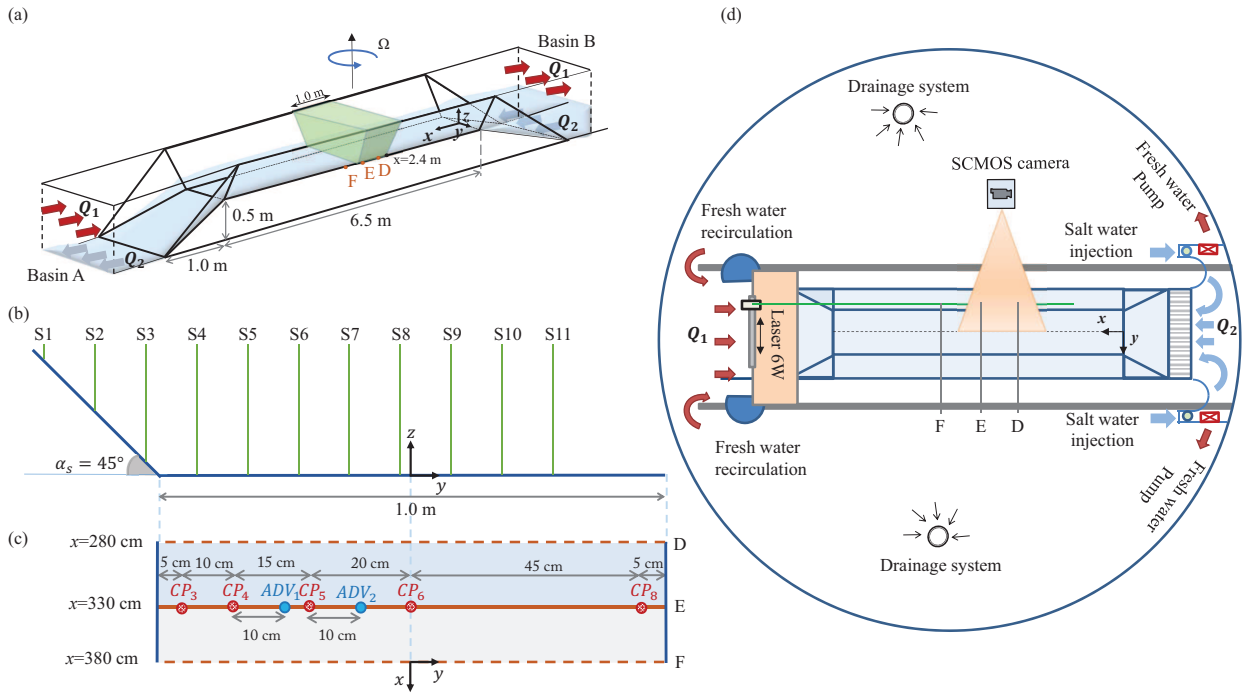

FIG. 1. (a) 3D schematic representation of the channel positioned in the LEGI Coriolis Platform, the green volume represents the Particle Image Velocimetry (PIV) measurement domain. (b) Trapezoidal channel side view and PIV fields of view (green vertical lines), (c) plan view of the central portion of the channel and cross-channel conductivity probes (CP) locations, (d) schematic plan view of setup in the Coriolis rotating tank.

ern hemisphere (Fig.1d). A straight, trapezoidal cross-section sill channel of length 6.5 m (Fig.1a) was positioned in the tank. This channel was constructed in transparent acrylic to facilitate flow visualization. Entry and exit slopes ($\alpha_b = 26.57°$) connected the main raised sill channel section to the deeper inlet (B) and outlet (A) basins. The trapezoidal cross-section had a 2 m top width (W_t) and 1 m bottom width (W_b), with side slopes of $\alpha_s = 45°$, and could be submerged to a maximum depth of 0.5 m (Fig.1b).

At the beginning of each experiment the circular tank was filled with freshwater of density ρ_1, to a total depth $H = 0.9$ m, with a corresponding submergence depth in the trapezoidal channel $H_{ch} = 0.4$ m. In Fig.1, the Cartesian coordinate system (x, y, z) is shown such that the origin (0,0,0) lies at the centerline of the trapezoidal channel bed, adjacent to Basin B (Fig.1a). The non-dimensional coordinate system is (x^*, y^*, z^*), where $x^* = x/W_b$, $y^* = y/W_b$ and $z^* = z/H_{ch}$. By convention the terms 'right-hand side' and 'left-hand side', will be used with reference to an

observer looking along the channel, in the direction of the lower saline water flow propagation.

For the rotating experiments, the platform was spun-up slowly to reach a fixed angular velocity Ω and attain a state of rigid body rotation after several hours (Linden and Heijst, 1984). The saline water of density ρ_2 was delivered through a gravity feed system to the bottom of basin B, via a rectangular inlet manifold, filling up basin B slowly (to minimize initial mixing) until the dense water interface reached the elevation of the trapezoidal channel bottom. At this point, a prescribed, constant saline water discharge Q_2 was fed into basin B to establish a stable, dense bottom water flow along the trapezoidal channel. The same flow rate was then extracted from outlets at the tank floor, ensuring maintenance of a constant water depth in the basin and channel. Once the saline water outflow was fully established through the channel and outflowing from basin A, two water pumps located in the upper part of Basin B were utilised to generate a recirculation flow that provided a constant fresh water flux Q_1 into Basin A, to establish a stratified exchange flow within the trapezoidal channel. Experimental measurements were targeted at obtaining high resolution density and velocity fields at different transverse sections across the channel width. These measurements focused on the central 1 m-long section of the 6.5 m long trapezoidal channel (Fig.1a, i.e. 240 cm $< x <$ 340 cm, well away from the converging and upsloping approaches from basins A and B). This central channel region was selected to ensure that the exchange flow conditions generated through this section were the most likely to be fully geostrophically adjusted (as discussed later) under rotating flow conditions.

Two-dimensional Particle Image Velocimetry (2D PIV) was used to obtain measurements of the velocity field in vertical (XZ) planes along this central region of the trapezoidal channel (Fig.1b). A 6 W YAG laser, mounted on a traverse system on the side of the tank, provided a vertical laser sheet, aligned parallel to the x axis, that could be positioned transversely across the channel width. This set-up allowed the measurement of synoptic velocity fields in 11 vertical (XZ) planes at lateral positions ranging between -79.2 cm $< y <$ 20.8 cm, with a cross-channel distance between each vertical plane of 10 cm (see Fig.1b). This allowed velocity measurements to be obtained in a region of $y = 1$ m width in the right hand side of the channel looking downstream, thus in the region where the dense current is expected to be displaced under Coriolis force in the circular tank rotated in a anti-clockwise direction. Velocity fields were acquired using a SCMOS camera (PCO edge s-s), with a spatial resolution of 2560x2160 pixels at a frame rate of 20 Hz. The PIV measurements were performed by scanning the 11 vertical sections 3 times for a 30 s measurement time, for each plane. The time elapsed between individual PIV scans obtained at the same mea-

surement section (namely between Scans 1,2 and 3) was 6 min. The synoptic velocity fields were then calculated using a cross-correlation PIV algorithm (UVmat, LEGI, Grenoble, http://coriolis.legi. grenoble-inp. fr).

Vertical profiles of the density field were obtained using 5 micro-conductivity probes (MSCTI, PME Vista USA) positioned on a transect arm spanning across the trapezoidal channel (Fig.1c) and overlapping the central area of interest and velocity fields at 3 locations, namely Section D, E and F (respectively at $x = 280$ cm, $x = 330$ cm and $x = 380$ cm, Fig.1c). One side-looking and one down-looking Acoustic Doppler Velocimeter (ADV) were positioned with their sampling volumes at an equivalent vertical elevation to the micro-conductivity probes tips to collect coupled velocity profiles.

Within all experiments, the saline water flow rate Q_2 was kept constant (i.e. $Q_2 = 4.4\ 1\cdot \mathrm{s}^{-1}$), while the flow rate of the fresh water Q_1 was varied over a range of values to generate both uni- (i.e. $Q_1 = 0$) and bi-directional exchange flows with different net-barotropic forcing in the upper fresh water layer (Q_1 =8 and $20\ 1\cdot \mathrm{s}^{-1}$). The rotation period T of the Coriolis Platform was varied and four angular velocities $\Omega = 2\pi/T = 0, 0.03, 0.05, 0.1$ rad$\cdot \mathrm{s}^{-1}$, were tested (with Coriolis parameter $f = 2\Omega$=0, 0.06, 0.1 and 0.2 rad$\cdot \mathrm{s}^{-1}$). The density difference of fresh and saline water flows was maintained constant at $\Delta\rho \simeq 10\mathrm{kg}\cdot \mathrm{m}^{-3}$.

The relevant non-dimensional parameters are given in Table I where a summary details of the experiments undertaken and the main variables are reported. The densimetric Froude number for the lower dense outflow layer is given by $Fr_2 = \tilde{U}_2/\sqrt{g'_0\tilde{h}_2}$, where $\tilde{U}_2$ and $\tilde{h}_2$, are the mean velocity and depth controlling the hydraulic regime of the dense layer and $g'_0 = g\Delta\rho/\rho_1$ is the reduced gravity based on the density difference between the layers $\Delta\rho$, and g is the gravitational acceleration. The non-dimensional parameters related to rotation are the Rossby number $Ro = \tilde{U}_2/f\widetilde{W}$ and the Burger number $Bu = R/\widetilde{W}$ (Rabe et al., 2007), where $\widetilde{W}$ is the dense outflow interfacial width, a function of its depth $\tilde{h}_2$ as $\widetilde{W} = W_b + 2\tilde{h}_2$ and R is the Rossby radius of deformation defined as $R = \sqrt{g'_0\tilde{h}_2}/f$. An additional parameter of importance to rotating channel flows is the Ekman number, $Ek = 2\nu/(f{H_{ch}}^2)$ representing the frictional effects induced at the boundaries (i.e. bed and interface) by Coriolis accelerations, with a frictional boundary layer scaling as $\delta_{Ek} = Ek^{1/2}H$. The stability of the interface between the two layers is expressed in terms of the bulk Richardson number $Ri = g'\delta/(\Delta U)^2$ based on the local reduced gravity g' (see Eq.3), the velocity shear layer thickness δ and the velocity difference between the upper and lower layer ΔU, which will be discussed in Sec.III D. Finally, turbulent conditions are assured by the overall Reynolds num-

ber $Re = \sqrt{g'_0 H_{ch}} H_{ch}/\nu$ being of the order of $80,000$ and the integral scale Reynolds number $Re_{l_0} = {u'_2}^2 \sqrt{(15/\nu\varepsilon)}$ based on the turbulence dissipation scale $\varepsilon = {u'_2}^3/\tilde{h_2}$, being $130 < Re_{l_0} < 250$ in the present experiments. The main parameters investigated in the experimental runs are thus (i) the relative magnitude of fresh and saline inflow volume fluxes $q^* = Q_1/Q_2$, (ii) the Coriolis parameter f and (iii) the Burger number Bu.

TABLE I. Experimental parameters in laboratory study and important non-dimensional quantities

Run	Q_1	q^*	f	$\tilde{U}_2$	$\tilde{h}_2$	Ro	R	Fr_2	Bu	Ri	Ek
	$(\mathrm{l}\cdot\mathrm{s}^{-1})$	(-)	$(\mathrm{rad}\cdot\mathrm{s}^{-1})$	$(\mathrm{m}\cdot\mathrm{s}^{-1})$	(m)	(-)	(m)	(-)	(-)	(-)	(10^{-3})
B1O	0	0	0	0.04	0.1	–	–	0.40	–	0.80	–
B1A	8	1.8	0	0.04	0.09	–	–	0.43	–	0.58	–
B1B	20	4.5	0	0.04	0.09	–	–	0.43	–	0.28	–
B2O	0	0	0.06	0.04	0.12	0.51	1.73	0.37	1.39	0.80	0.18
B2A	8	1.8	0.06	0.04	0.1	0.53	1.58	0.4	1.31	0.36	0.18
B2B	20	4.5	0.06	0.03	0.09	0.41	1.50	0.32	1.27	0.20	0.18
B3O	0	0	0.1	0.05	0.1	0.40	0.95	0.51	0.79	0.64	0.11
B3A	8	1.8	0.1	0.04	0.1	0.32	0.95	0.40	0.79	0.34	0.11
B3B	20	4.5	0.1	0.03	0.09	0.24	0.90	0.32	0.76	0.23	0.11
B4O	0	0	0.20	0.06	0.13	0.22	0.54	0.53	0.43	0.88	0.05
B4A	8	1.8	0.20	0.03	0.09	0.12	0.45	0.32	0.38	0.55	0.05
B4B	20	4.5	0.20	0.02	0.05	0.09	0.33	0.29	0.30	0.35	0.05

III. RESULTS: DYNAMICS OF UNI AND BI-DIRECTIONAL EXCHANGE FLOWS

A. Velocity Fields

Fig.2 shows, for non-rotating ($f = 0$ rad $\cdot$ s^{-1} i.e. run B1, Table I) flow conditions, the time averaged, synoptic velocity fields generated under different net-barotropic flow conditions (i.e. $q^* = 0$ in Fig.2a, $q^* = 1.8$ in Fig.2b and $q^* = 4.5$ in Fig.2c). The background color map details the magnitude of the horizontal time-averaged velocity component u at PIV section S9, i.e. approximately along the channel centerline (see Fig.1b). Increasing Q_1 results in a reduction of the non-

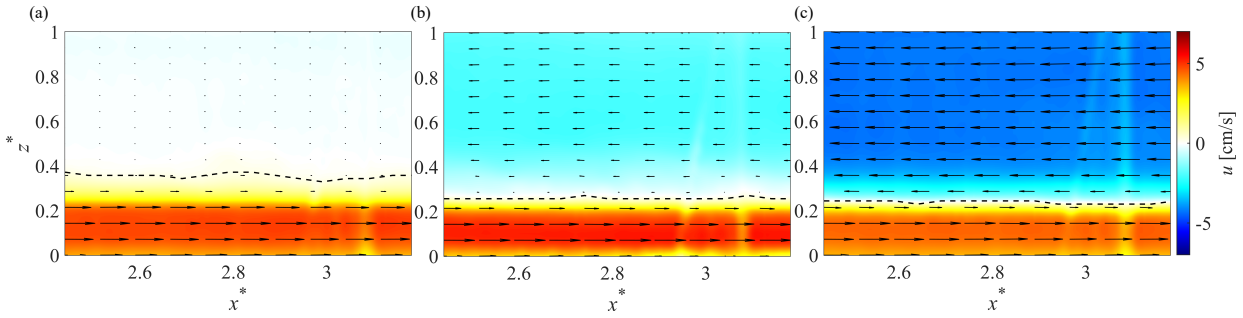

FIG. 2. Time-averaged, synoptic (XZ) velocity vector fields at channel centerline (i.e. section S9, Fig.1b) showing colormap of the magnitude of u for non-rotating (i.e. $f = 0$ rad $\cdot$ s^{-1}) runs (a) B1O with $q^* = 0$ (i.e. uni-directional exchange flow) (b) B1A with $q^* = 1.8$ and (c) B1B with $q^* = 4.5$ (i.e. bi-directional exchange flow).

dimensional lower saline layer thickness $h_2^* = h_2/H_{ch}$, with h_2 defined as the elevation at which the streamwise velocity is 5% of the maximum streamwise velocity in the lower layer, for the uni-directional exchange flow experiments (Davarpanah Jazi et al., 2020) and as the zero-velocity interface, for the bi-directional exchange flows. In Fig.2a-c, h_2^* is represented by the black dashed line. A slight increase of the maximum lower layer velocity $U_{2,max}$, from $U_{2,max}$ =5.0 cm $\cdot$ s^{-1} for the run B1O, to $U_{2,max}$ =5.4 cm $\cdot$ s^{-1} for the run B1A (i.e. $q^* = 1.8$), is found in Fig.2b, as a consequence of the lowering of h_2^* induced by the net-barotropic, upper fresh water on the lower saline water outflow. By contrast, a reduction in the lower layer maximum velocity $U_{2,max}$ =4.7 cm $\cdot$ s^{-1} for highest barotropic condition $q^* = 4.5$ is also observed in Fig.2c, despite the depletion of h_2^*. The reduction of both the lower layer velocity and h_2^* implies that an overall reduction of the lower layer flux in the channel must occur. This first indication of the effect of net barotropic forcing in upper layer on bottom saline outflow will be discussed in detail in the following Part III E where fresh and saline water fluxes in the trapezoidal channel are evaluated and discussed.

The influence of rotation on the transverse distribution of along-channel velocity in the trapezoidal cross-section is highlighted in Fig.3. Contour plots of the time averaged velocity $u(y,z)$ measured at $x^* = 2.8$ are presented for different f values and with $q^* = 0$. The rotation induces, as expected, a geostrophic adjustment of the lower outflowing layer and a larger cross-channel variation in $h_2{}^*$, represented by the black dotted lines in Figs.3a-d. As f increases an overall increase of $h_2{}^*$ is observed, particularly in the vicinity of the inclined side slope of the trapezoidal channel (i.e. $y^* = -0.5$), with respect to the channel center line (i.e. $y^* = 0$), although the velocity structure in

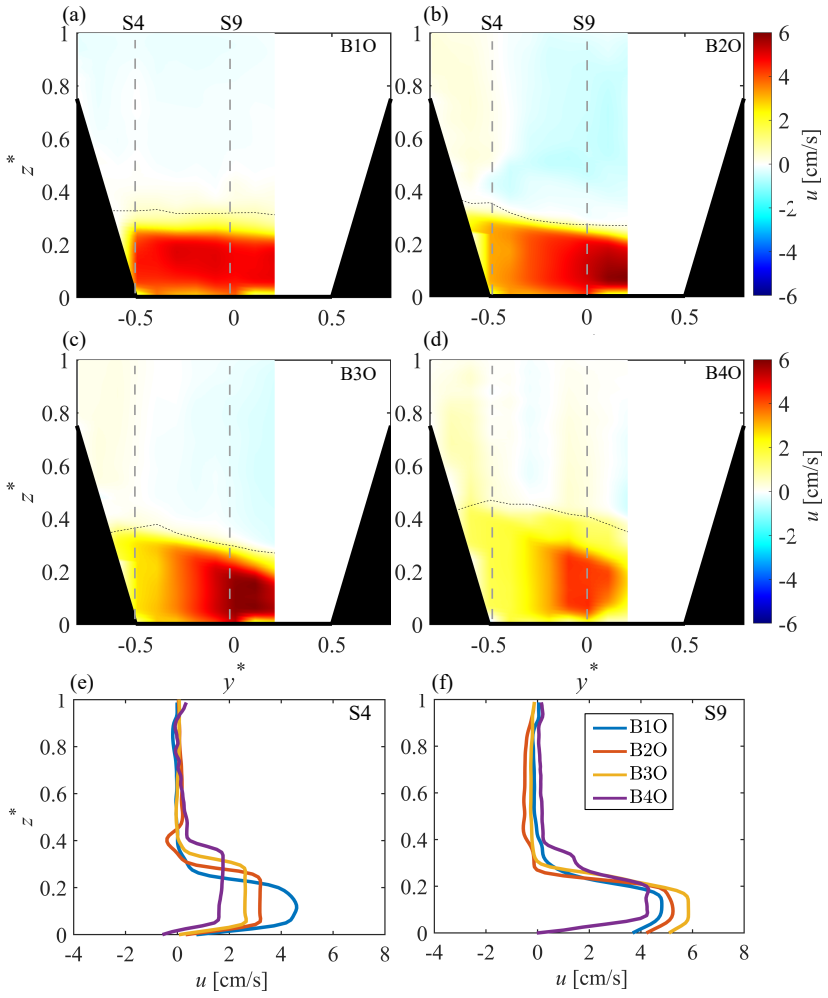

FIG. 3. Cross channel colormap of the time averaged, along-channel velocity component $u(y,z)$, for $q^* = 0$ and different angular velocity: (a) $f = 0$, (b) $f = 0.06$ rad$\cdot$s^{-1}, (c) $f = 0.1$ rad$\cdot$s^{-1} and (d) $f = 0.2$ rad$\cdot$s^{-1}. Note that the perspective is upstream, and hence a deflection to the left-hand side means a deflection to the right-hand side from the downstream perspective, which is used as a reference. Individual profiles of $u(y,z)$ are shown at section S4 (e) and section S9 (f) for comparison purposes.

the lower layer also appears to become less well defined at higher f values, expecially for $f = 0.2$ rad$\cdot$s^{-1} (Fig.3d). The increase in $h_2{}^*$ is coupled with a decrease in the magnitude of the along-channel velocity u_2 of the dense bottom layer in the y^* direction (from section S9 in Fig.3f at the center of the channel, at $y^* = 0$, to section S4 in Fig.3e near the sloping side wall of the channel, at $y^* = -0.5$). As the rotation rate increases, the high velocity region of the lower outflowing dense layer is shown to migrate from the right hand side of the channel ($y^* < 0$ in Fig.3a) to a more centre line location ($y^* > 0$ in Fig.3b-c) from a downstream looking perspective, while diminishing

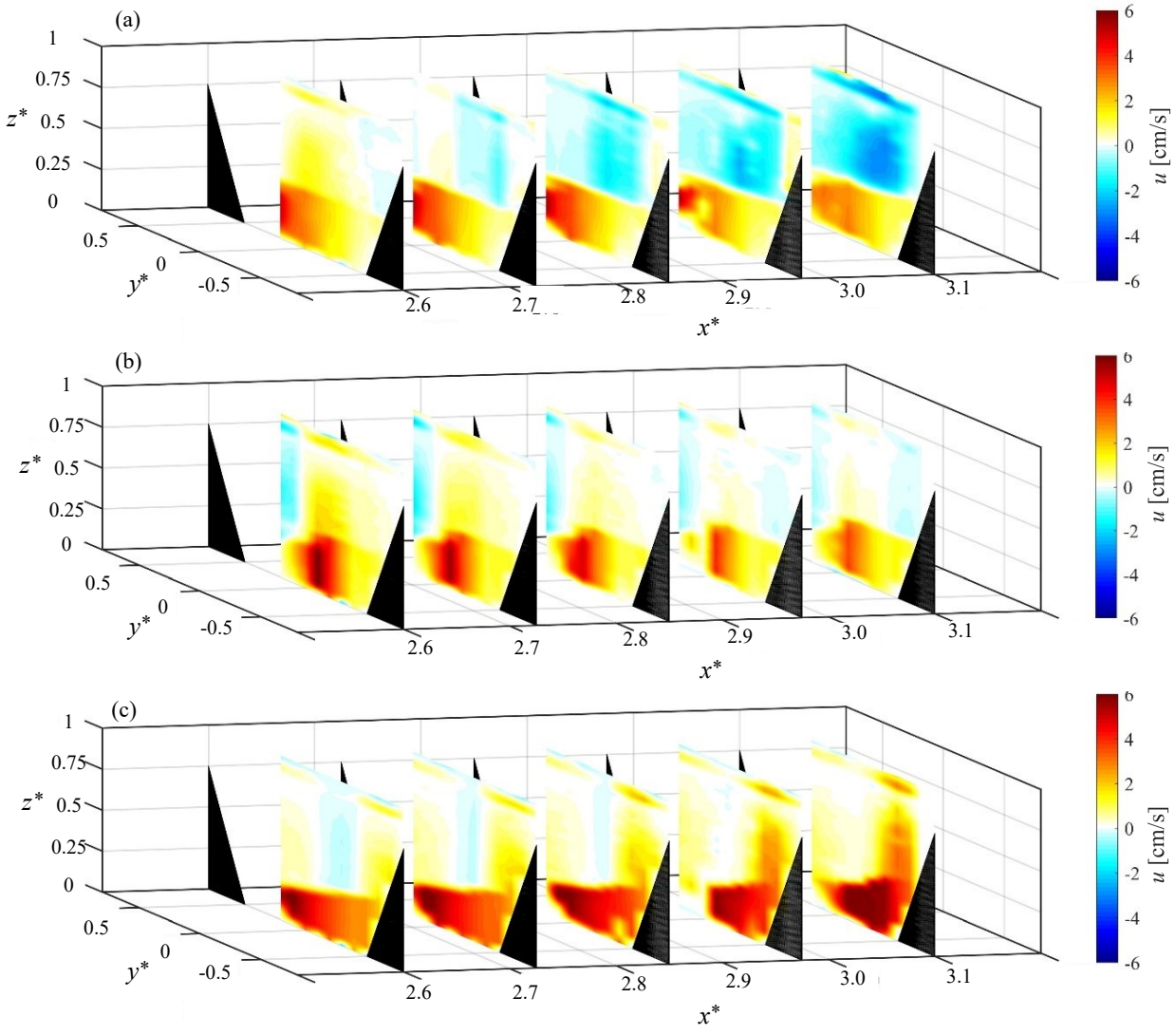

FIG. 4. 3D Cross channel colormap of the time averaged, along-channel velocity component $u(y,z)$ of run B4O with $q^* = 0$ and $f = 0.2$ rad $\cdot$ s^{-1}, for successive PIV scans at (a) $t = 0$, (b) $t = 6$ min and (c) $t = 12$ min.

significantly in overall magnitude at the highest rotation rate, i.e. when $f = 0.2$ rad $\cdot$ s^{-1} (Fig.3d). It is also interesting to note that the along-channel velocity magnitude in the lower layer at S4 (i.e. $y^* = -0.5$) also reduces significantly as the rotation rate increases (Fig.3e). By contrast, at section S9 the maximal velocity $U_{2,max}$ increases from $U_{2,max} \simeq 4.8$ cm $\cdot$ s^{-1} in the non-rotating run B1O, to $U_{2,max} \simeq 5.2$ and 5.8 cm $\cdot$ s^{-1} rispectively in rotating runs B2O and B3O (i.e. $f = 0.06$ and 0.1 rad $\cdot$ s^{-1}, respectively), before reducing to $U_{2,max} \simeq 4.3$ cm $\cdot$ s^{-1} for $f = 0.2$ rad $\cdot$ s^{-1} (run B4O, Table I). These individual parametric effects of rotation are also shown in Fig.3e,f displaying time

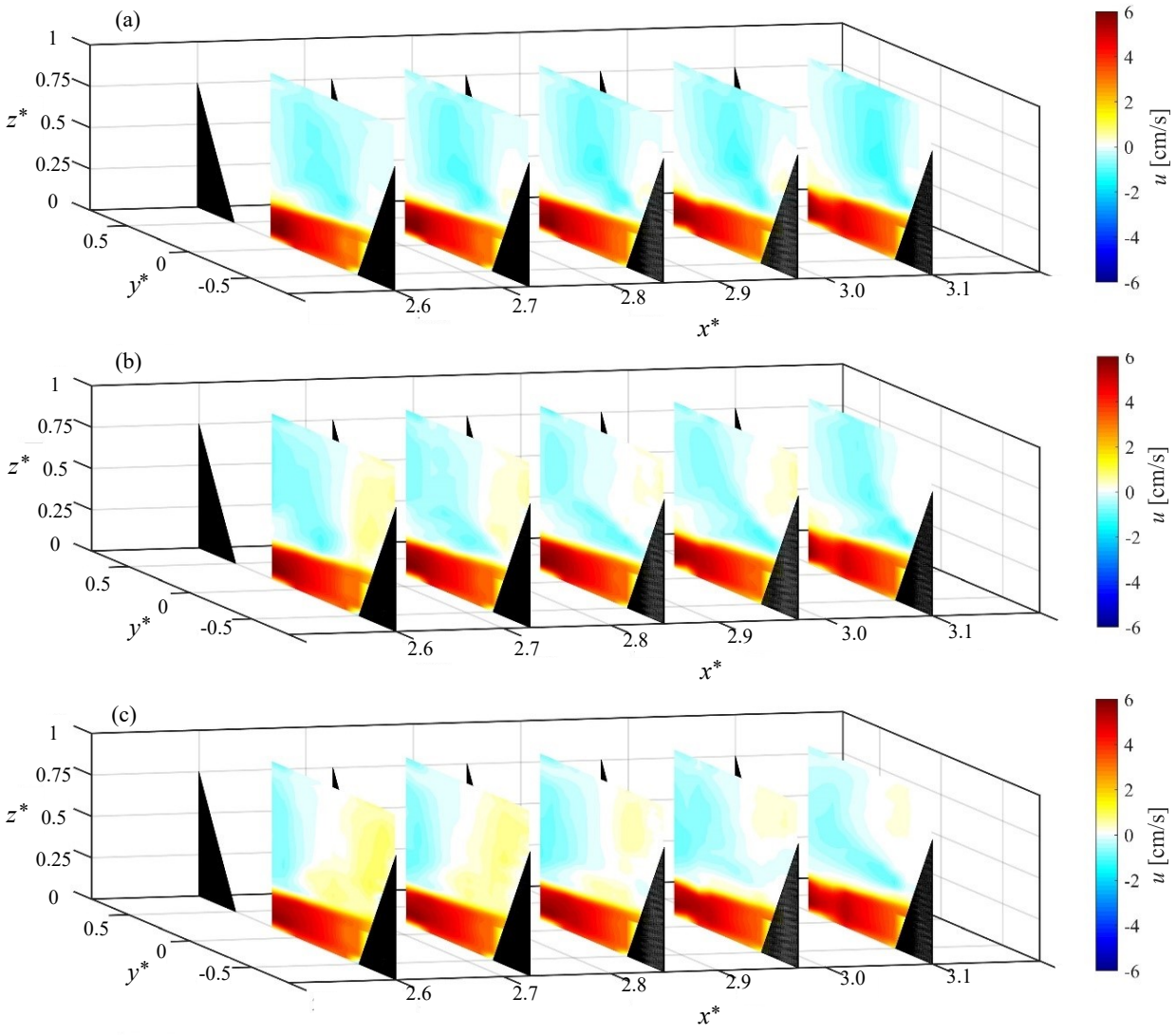

FIG. 5. 3D Cross channel colormap of the time averaged, along-channel velocity component $u(y,z)$ of run B2O with $q^* = 0$ and $f = 0.06$ rad $\cdot$ s^{-1}, for successive PIV scans at (a) $t = 0$, (b) $t = 6$ min and (c) $t = 12$ min.

averaged velocity profiles at sections S4 and S9 for the different f values tested.

The marked reduction in $U_{2,max}$ at the highest Coriolis parameter ($f = 0.2$ rad $\cdot$ s^{-1}, run B4O, Table I) also appears to be associated with an unsteady velocity structure of the lower dense water layer. This is in agreement with the study of Rabe et al. (2007), who found that lock-exchange flows through a width-constricted channel were characterized by an unsteady flow with a meandering propagation and the formation of eddies within the channel when $Bu < 0.5$. In the uni-directional exchange flow condition generated in run B4O, $Bu < 0.5$ (Table I) and the time-variability and

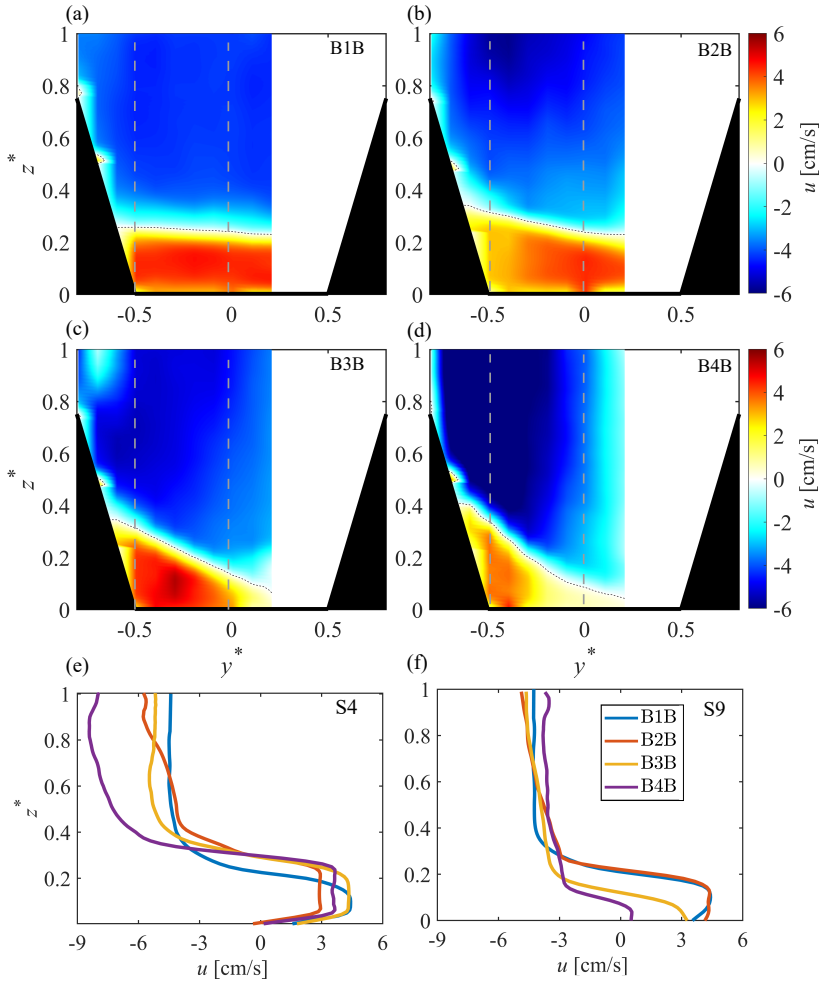

FIG. 6. Cross channel colormap of the time averaged, along-channel velocity component $u(y,z)$, for $q^* = 4.5$ and different angular velocity :(a) $f = 0$ rad $\cdot$ s^{-1}, (b) $f = 0.06$ rad $\cdot$ s^{-1}, (c) $f = 0.1$ rad $\cdot$ s^{-1} and (d) $f = 0.2$ rad $\cdot$ s^{-1}. Note that the perspective is upstream, and hence a deflection to the left-hand side means a deflection to the right-hand side from the downstream perspective, which is used as a reference. Individual profiles of $u(y,z)$ are shown at section S4 (e) and section S9 (f) for comparison purposes.

baroclinic instability generated in the outflowing dense layer, is shown in Fig.4, displaying various 2D PIV sections in x, of each of the 3 PIV scans taken (namely Scan 1 in Fig.4a , Scan 2 in Fig.4b and Scan 3 in Fig.4c) during run B4O. Large variability both in the upper and lower layer velocities is found, as well as the corresponding layer thicknesses, which prevents accurate determination of the velocity interface between the two layers. Specifically, the high velocity region of the lower outflowing dense layer is observed to migrate from the left hand side of the channel ($y^* > 0$) in the first scan, to a more centre line location ($y^* = 0$), in the second scan and finally

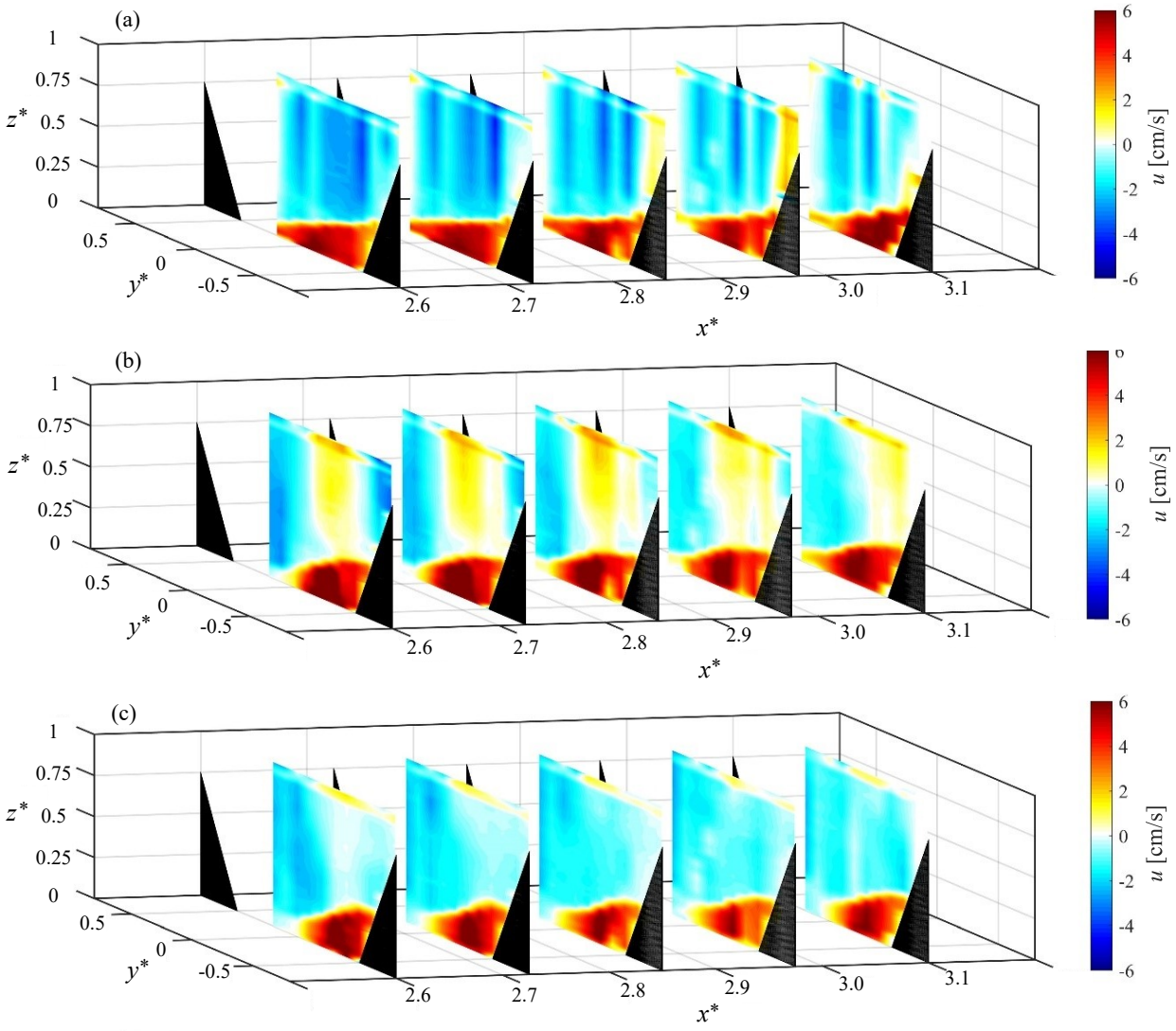

FIG. 7. 3D Cross channel colormap of the time averaged, along-channel velocity component $u(y,z)$ of run B4A with $q^* = 1.8$ and $f = 0.2$ rad $\cdot$ s^{-1}, for successive PIV scans at (a) $t = 0$, (b) $t = 6$ min and (c) $t = 12$ min.

to the right hand side of the channel ($y^* < 0$) in the third scan, from a downstream looking perspective. The variability in the outflowing lower layer is also accompanied by a decrease in the upper layer minimum velocity $U_{1,min} = -4.3$ cm $\cdot$ s^{-1} up to -0.9 cm $\cdot$ s^{-1}, with an apparent fresh water flow reversal at the right hand side of the channel ($y^* < 0$) in the third PIV scan. Along with the observed variation in the lower layer thickness between the different PIV scans, the lateral variability in the position of the high velocity region is clearly indicative of unsteadiness in the outflowing dense water layer.

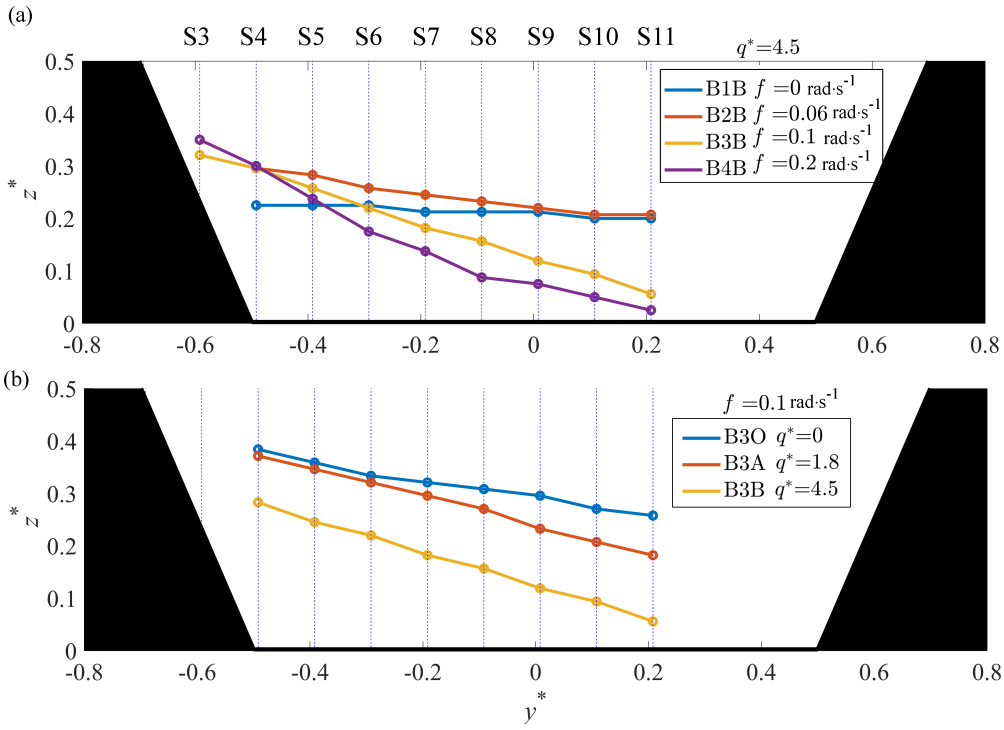

FIG. 8. Cross channel variation of zero-velocity elevation (i.e. $h_2{}^*$ layer thickness) in all the measured PIV sections, (a) for different f values tested and $q^* = 4.5$ and (b) for different q^* values tested and $f = 0.1$ rad $\cdot$ s^{-1}. Note that the perspective is upstream, and hence a deflection to the left-hand side means a deflection to the right-hand side from the downstream perspective, which is used as a reference.

For comparison, the corresponding 2D PIV plots for the 3 PIV scans taken in run B2O, are shown in Fig.5. For this particular run (characterized by a $Bu > 0.5$, Table I), the velocity structure of the dense water outflow is clearly steady in both space and time, as there is not a noticeable variability either between individual scans or in the along-channel direction within each scan.

The additional influence of net-barotropic forcing in the upper fresh water layer is highlited in Fig.6 displaying contour plots of the transverse distribution of the along-channel velocity $u(y,z)$ in both layers, for different f values and $q^* = 4.5$. Selected time-averaged $u(y,z)$ velocity profiles at section S4 and S9 for varying f values, are shown in Fig.6e,f for comparison purposes. The lower layer velocity magnitude for the B1B experiments ($f = 0$, $q^* = 4.5$, Table I) is shown to be largely consistent across all transverse PIV sections analysed (Fig 6a), with a maximum velocity $U_{2,max} = 4.6$ m $\cdot$ s^{-1}. An increase of f again results in an increasing inclination of zero-velocity interface between the counter-flowing layers, which also appears to be enhanced by the net-barotropic flow conditions imposed by the upper freshwater layer (i.e. larger q^* value, Fig.6b-

d). This coincides with a shift in the maximum velocity in the upper fresh layer towards the right hand side of the channel and a reduction in the maximum velocity in the lower saline layer as f increases, when compared to the equivalent uni-directional exchange flow runs ($q^* = 0$ in Fig.3a-d), thus highlighting the effect of the upper fresh water flux on the internal flow dynamics. In particular, when $f > 0.1$ rad $\cdot$ s^{-1}, the saline lower layer thickness is found to diminish almost completely at $y^* > 0$ (Fig.6c,d,f). In particular, for run B4B in Fig.6d, the complete reduction of the saline lower layer thickness and velocity u_2 at $y^* > 0$ is expected to be indicative of a significant reduction in the lower layer flux, with implications for the geostrophic adjustment of the dense outflow. As previously discussed, in the experiments B4B (Fig.6d) and B4A (Fig.7), with $Bu < 0.5$ (see Table I), the stratified exchange flow appears to be less stable (both spatially and temporally), with greater variability in both the dense and upper fresh layers. The 2D PIV plots for the 3 PIV scans taken in run B4A, are shown in Fig.7 and display the variability in the counter-flowing water masses, with the complete reduction of the saline lower layer thickness at $y^* > 0$ in Scan 2 in Fig.7b and Scan 3 in Fig.7c. In the following sections, the implications of rotation and net-barotropic forcing on the geostrophic adjustment in the outflow dense layer, as well as the generation of baroclinic instabilities observed within uni- and bi-dirctional exchange flow runs where $Bu < 0.5$, will be examined in more detail.

The cross channel variation of normalised lower layer thickness ${h_2}^*$ is shown for the four rotation conditions and for different net-barotropic forcing conditions in Fig.8a and b respectively. It is observed in Fig.8a, that as f increases initially (i.e. $f = 0 \rightarrow 0.06$ rad $\cdot$ s^{-1}), an increase in ${h_2}^*$ is observed especially towards the sloping side wall of the channel. However, with a further increase in f (i.e. $f = 0.1$ and 0.2 rad $\cdot$ s^{-1}), the thickness ${h_2}^*$ reduces in the majority of the channel, except on the channel side slope, as the geostrophic slope of the zero-velocity interface, becomes progressively steeper (i.e. as f increases). Likewise, in Fig.8b, the increase of q^* results in an overall reduction in both layer thickness ${h_2}^*$ and a slight increase in interface inclination. The velocity interface defined by the $u = 0$ (or 5%) elevation, will be compared with the geostrophic slope α_g in Part III C, to investigate the geostrophic adjustment of the dense water outflow under the influence of both background rotation and net-barotropic forcing.

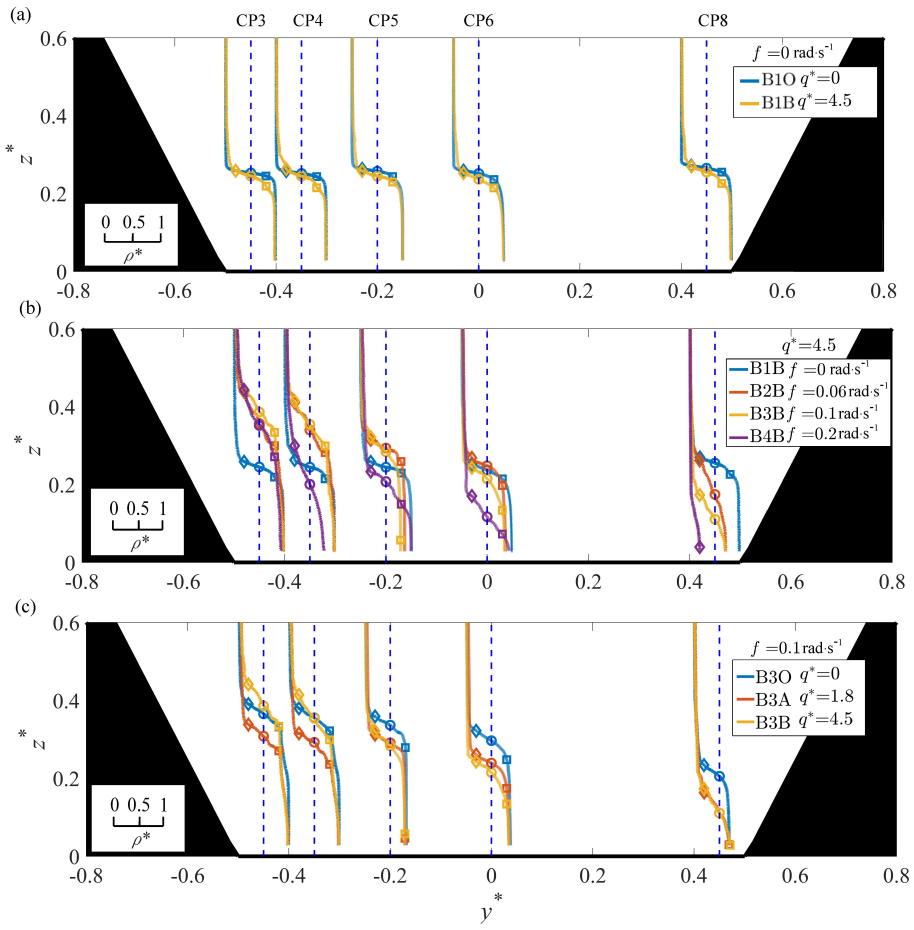

FIG. 9. Normalized density profiles ρ^* across the trapezoidal channel plotted versus the dimensionless total water depth z^* for transverse probes CP3, CP4, CP5, CP6 and CP8.

B. Density profiles

The density profiles for the uni and bi-directional stratified exchange flows were measured by conductivity probes at $x = 280$ cm, 330 cm and 380 cm (i.e. locations D,E and F, Fig.1a,c), with five probes distributed in y (as shown in Fig.1c). The dimensionless density excess ρ^* is defined as:

$$\rho^* = \frac{\rho(z) - \rho_1}{\rho_2 - \rho_1} \tag{1}$$

where $\rho^* = 0$ and $\rho^* = 1$ represent the unmixed freshwater and saline water densities, respectively. In Fig.9, density excess ρ^* profiles, averaged between the three measurement locations D,E and F, are plotted versus the non-dimensional water depth z^*. For each ρ^* profile, the elevation of the $\rho^* = 0.2, 0.5$ and 0.8 isopycnals are shown as diamond, circle and square markers, respectively.

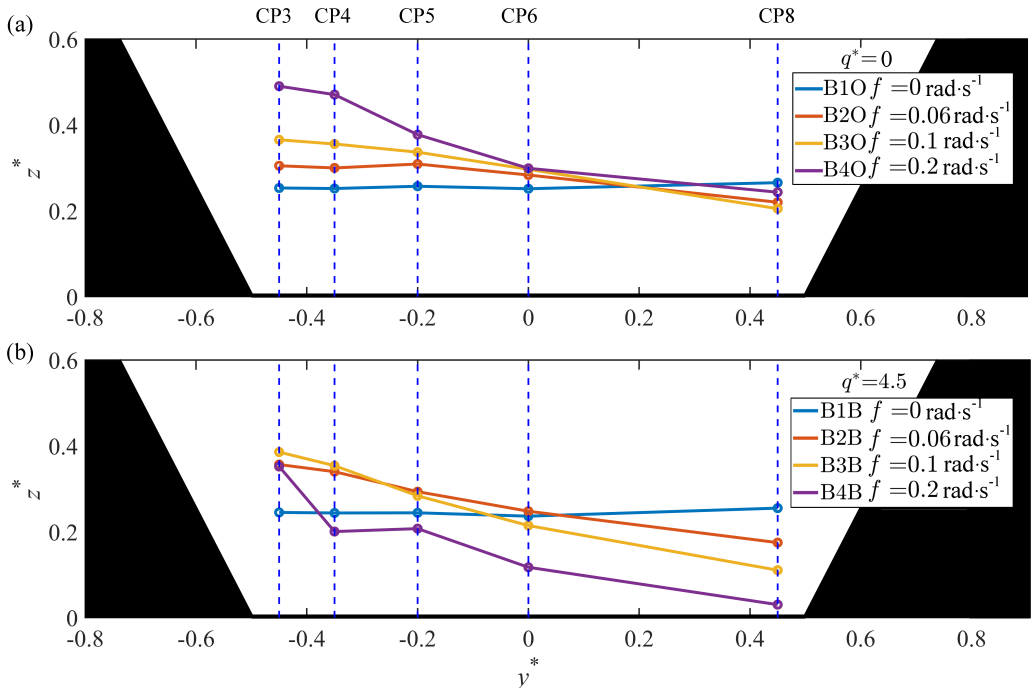

FIG. 10. Cross channel elevation of the $\rho^* = 0.5$, for different f and (a) $q^* = 0$ and (b) $q^* = 4.5$.

For the non-rotating runs in Fig.9a, an increase of $q^* = 4.5$ (B1B, yellow line) generates a slight overall decrease of the interfacial elevation of $\rho^* = 0.5$ compare to the uni-directional exchange flow generated when $q^* = 0$ (B1O, blue line). The elevation of $\rho^* = 0.5$ for the run B1O ($f = 0$, $q^* = 0$) is constant for all the profiles along y^*, as expected, with a very strong pycnocline observed due to minimal interfacial mixing, resulting in little vertical variation between the $\rho^* = 0.2, 0.5$ and 0.8 isopycnal elevations. For the stratified exchange flow generated in run B1B (i.e. as q^* is increased), the larger vertical separation measured between the $\rho^* = 0.2$ and 0.8 isopycnals is indicative of an increase in shear-generated mixing between the counter-flowing fresh and saline layers. As such, the difference between the elevation of the isopycnal $\rho^* = 0.2$ and the isopycnal $\rho^* = 0.8$, provides also an indication of the shear mixing layer thickness. Thus, the increase in the mixing layer thickness and reduction in interfacial elevation for $q^* = 4.5$ (under non-rotating conditions) is due entirely to the interfacial entrainment of lower dense water into the counter-flowing upper fresh water layer.

Fig.9b presents similar dimensionless density profiles ρ^* for different f values and $q^* = 4.5$. As f increases ($f = 0 \rightarrow 0.1$ rad $\cdot$ s^{-1}), a general increase of the $\rho^* = 0.5$ elevation is observed at $y^* < 0$ probe locations (i.e. on the right side of the channel from a downstream perspective), while a significant reduction in $\rho^* = 0.5$ elevation is shown at $y^* > 0$. This is indicative of the

increasing transverse inclination of the density interface resulting from geostrophic adjustment of the outflowing dense water layer. It is also noted that when the rotation rate is increased to its highest level (i.e. $f = 0.2$ rad $\cdot$ s^{-1}, $Bu = 0.3$), the $\rho^* = 0.5$ interface shows a marked reduction across the channel width and is not identified at the left hand side of the channel (i.e. location CP8), where the dense water current is largely absent. The mixing layer thickness (again represented by the elevation difference between the $\rho^* = 0.8$ and $\rho^* = 0.2$ isopycnals) is also observed to increase with increasing f across the full channel width (i.e. CP8 $\rightarrow$ CP3), although the $\rho^* = 0.2$ isopycnal elevation at CP8 is not identified for rotating runs with $f > 0$. It is noted that, under certain circumstances, previous studies have indicated that rotation can act to suppress turbulent mixing (e.g., Maxworthy, 1986; Wells, 2007; Cenedese et al., 2004), induced by shear-driven interfacial instabilities (e.g. Kelvin-Helmholtz billows or Holmboe waves), which are considered to be a main mechanism for mixing and entrainment in stratified exchange flows. However, recent studies suggest that these may be enhanced in the presence of rotation by the large scale Ekman-driven secondary circulations generated in the counter-flowing saline and fresh water masses (Darelius, 2008; Umlauf et al., 2010).

Likewise within Fig.9c, the normalized density profiles ρ^* across the channel, shown for $f = 0.1$ rad $\cdot$ s^{-1} and increasing q^* values, highlight two distinct behaviours. For $q^* = 1.8$ (run B3A, Table I), the dominant mechanism in the stratified exchange flow behaviour is the net-barotropic forcing in the upper fresh flow. Thus, in accordance with Fig.9a ($f = 0$ rad $\cdot$ s^{-1}), an overall decrease of the $\rho^* = 0.5$ isopycnal elevation is found. By contrast, for $q^* = 4.5$, the influence of rotation appears to be enhanced by the larger net barotropic forcing condition, with the $\rho^* = 0.5$ isopycnal elevation increased on the right side of the channel (i.e. $y^* < -0.4$), when compared to the rotating uni-directional exchange flow condition (i.e. blue circles, $q^* = 0$), but significantly reduced elsewhere. This again indicates that the transverse interfacial inclination of the density interface due to geostrophic adjustment is enhanced by increased barotropic forcing within the upper fresh water layer (i.e. as q^* increases). In addition, as observed in Fig.9b, a diluted bottom layer (i.e. $\rho^* < 1$) is measured at CP8, along with a general increase of the mixing layer thickness (defined again by the elevation difference between the $\rho^* = 0.8$ and $\rho^* = 0.2$ isopycnals) for increasing q^* values.

The transverse adjustment in the density interface is shown in Fig.10, where the cross channel elevation of the $\rho^* = 0.5$ isopycnal, (i.e. $z_{\rho^*=0.5}$) is compared at all the transverse probe locations for different f and q^* values. Here, it is clearly shown that an increase of f within the uni-

directional exchange flow experiments (i.e. $q^* = 0$, Fig.10a) results in an increasing inclination of the density interface (defined by $z_{\rho^*=0.5}$) and an associated increase in the lower saline layer thickness at the right hand side of the channel (from a downstream perspective). The coupled effect of different f values and net-barotropic forcing in the upper fresh water layer (i.e. $q^* = 4.5$) on the $\rho^* = 0.5$ isopycnal elevation is also shown in Fig.10b. Here, an increase of q^* causes an increase of the isopycnal $\rho^* = 0.5$ inclination across the channel (compared to equivalent rotating $q^* = 0$ runs plotted in Fig.10a). This generally increases the $z_{\rho^*=0.5}$ elevation on the right hand side of the channel, with a corresponding reduction on the left hand side, looking downstream. For $f = 0.2$ rad $\cdot$ s^{-1}, however, the generation of rotating stratified exchange flow conditions under both strong net-barotropic forcing (i.e. at $q^* = 4.5$) and strong rotation results in a significant depletion of the dense bottom layer across the channel width and its complete absence at density profile CP8, when compared to the uni-directional exchange flow case (i.e. $q^* = 0$, Fig.10a). The density interface defined by the $z_{\rho^*=0.5}$ elevation, will be compared with the geostrophic slope α_g in the following Part III C, to discuss the geostrophic adjustment of the dense current under the influence of both background rotation and net-barotropic forcing.

C. Geostrophic balance in uni and bi-directional exchange flows

The interfacial slope between the upper fresh and lower saline water layers can be analysed to derive additional information on the geostrophic adjustment in the bottom uni-directional ($q^* = 0$) and bi-directional ($q^* > 0$) exchange flows. If the outflowing bottom dense current is in geostrophic balance, such that the transverse pressure gradient is balanced by the Coriolis term, the geostrophic slope α_g can be derived as:

$$\alpha_g = \frac{\left(\widetilde{U}_2 - \widetilde{U}_1\right) f}{g'} \tag{2}$$

where $\widetilde{U}_2$ and $\widetilde{U}_1$ are the mean flow velocities in the lower and upper layers (measured from PIV data obtained at $x = 300$ cm) and g' is the local value of reduced gravity term that can be evaluated from measured density profiles (Girton et al., 2006):

$$g' = \frac{g}{\rho_2 z_{\rho^*=0.5}} \int_0^{z_{\rho^*=0.5}} (\rho(z) - \rho_1) dz \tag{3}$$

where $\rho(z)$ is the local density profile. In particular, the elevation of the $\rho^* = 0.5$ isopycnal, $z_{\rho^*=0.5}$ is assumed to represent a good approximation of the density interface between the dense bottom

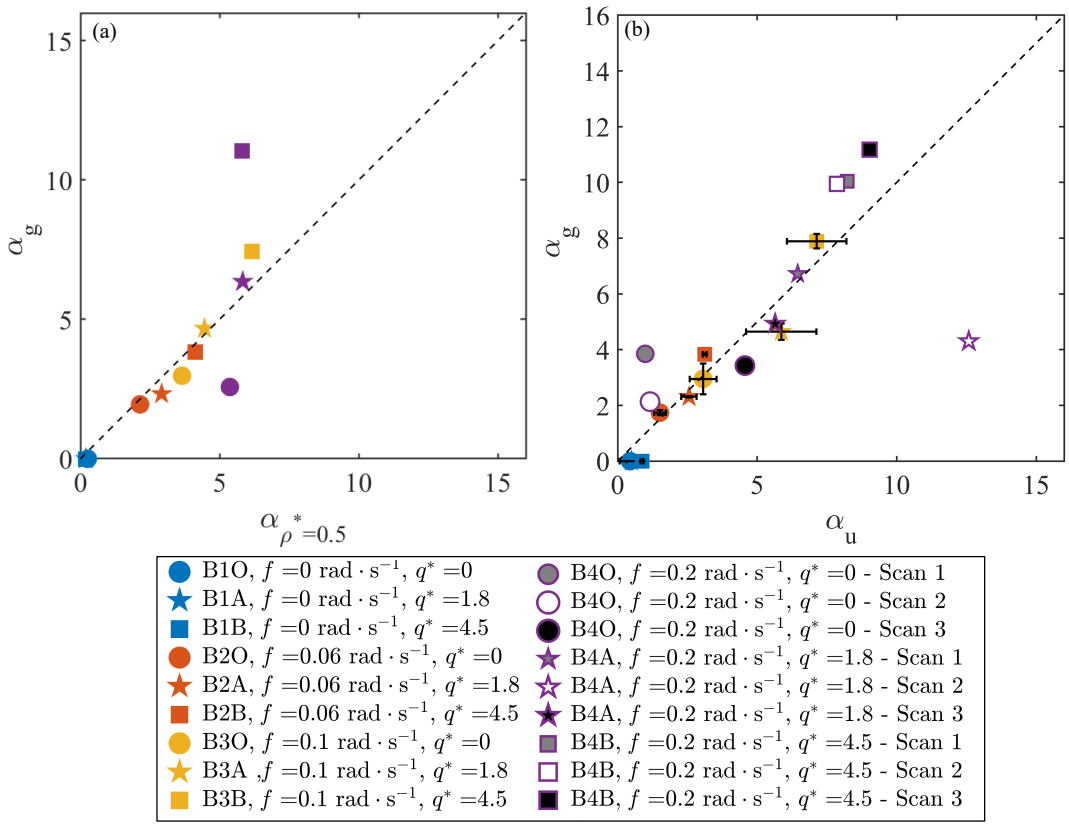

FIG. 11. Measured cross-channel interface slopes (a) $\alpha_{\rho^*=0.5}$ (taken at the transverse inclination angle of $\rho^* = 0.5$ isopycnal) and (b) α_u (taken at the transverse inclination angle of $u = 0$ for $q^* > 0$ and 5% interface for $q^* = 0$) plotted versus the calculated geostrophic slopes α_g

and fresh upper water layers (Cuthbertson et al., 2011). A comparison between the calculated α_g (Eq.2) and the measured cross-channel density interface angle $\alpha = \alpha_{\rho^*=0.5}$ (measured at the along-channel location $x = 300$ cm), is shown in Fig.11a. The latter has been evaluated as the gradient of the best linear fit (least squares) to the measured $z_{\rho^*=0.5}$ interface elevation. Overall, good agreement is found between α_g and $\alpha_{\rho^*=0.5}$ for $f < 0.2$ rad · s^{-1}, i.e. $Bu < 0.5$, suggesting that the dense bottom current and the fresh upper flow are largely in geostrophic balance for the experiments performed. As previously discussed, the cross-channel interface slope α, is influenced by the rotation and the increasing net-barotropic condition, as $\alpha_{\rho^*=0.5}$ increases for both larger f and q^* values. In bi-directional exchange flow runs B3B and B4B, the interface slope $\alpha < \alpha_g$, due to the combined effect of high rotation rate (i.e. $f > 0.1$ rad · s^{-1}) and large upper fresh water flow condition ($q^* = 4.5$) which provide the most effective disturbance to geostrophic adjustment of the stratified exchange flows. For experiments B4O and B4B, the deviation of the observed rotating-

channel stratified flow velocities from the geostrophic velocities in Fig.11a is reasonably due to the baroclinic instabilities observed experimentally for runs with $Bu < 0.5$ (Table.I), as previously discussed in Part III.

The velocity interface slope α_u obtained as the gradient of the best linear fit (least squares) to the measured zero velocity (or 5% for $q^* = 0$) elevation, is also compared to α_g in Fig.11b. In particular, for runs with $Bu > 0.5$, α_u is averaged between the PIV Scans 1-3 and error-bars display the variability, while for runs B4O, B4A and B4B with $Bu < 0.5$, α_u and α_g are shown for each Scan taken in the central region of PIV domain, i.e. $x^* = 2.8$. Fig.11b further confirm a good agreement between α_g and α_u for $f < 0.2$ rad$\cdot$s^{-1}, i.e. $Bu > 0.5$. The large variability in α_u for different scans taken in runs B4O and B4A also highlights the condition of baroclinic instability and unsteadiness in the outflowing dense water layer. Moreover, as discussed for the density interface, for $f > 0.2$ rad$\cdot$s^{-1}, i.e. $Bu < 0.5$, α_u largely deviates from the geostrophic slope α_g (Fig.11b). Specifically, in runs B4B and Scan 1 of B4O, $\alpha_u < \alpha_g$, while in Scan 2 of run B4A $\alpha_u >> \alpha_g$. This deviation indicates the presence of ageostrophic motions in the stratified flow with constant background vorticity. Ageostrophic motion such as unsteady meandering and gyre formation, which are not in geostrophic balance, appear due to baroclinic instability associated with space and time variability in velocity and density fields and turbulent mixing at the interface between the fresh and dense waters in the rotating system. Therefore, it is expected that rotating-channel turbulence observed in the large-scale laboratory facility is affected by these unsteady ageostrophic motions.

D. Shear and density layer thickness

The interfacial region between the dense lower and fresh upper layers is characterized by the shear layer thickness δ and the density layer thickness η, defined as (Zhu and Lawrence, 2001):

$$\delta = \Delta u / (du/dz)_{max} \tag{4}$$

$$\eta = \Delta \rho / (d\rho/dz)_{max} \tag{5}$$

where $\Delta u = U_{2,max} - U_{1,min}$ and $\Delta \rho = \rho_{2,max} - \rho_{1,min}$ are the local velocity and density differences between the two layers respectively. In weakly or stably stratified shear flows in which $\eta \geq \delta$, the primary mode of instability is the Kelvin–Helmholtz instability (KHI), consisting of a series of billows developing at the stratified exchange flow interface. Holmboe instability (HI) is expected to appear when the velocity shear layer thickness is larger than the density layer thickness $\delta > \eta$.

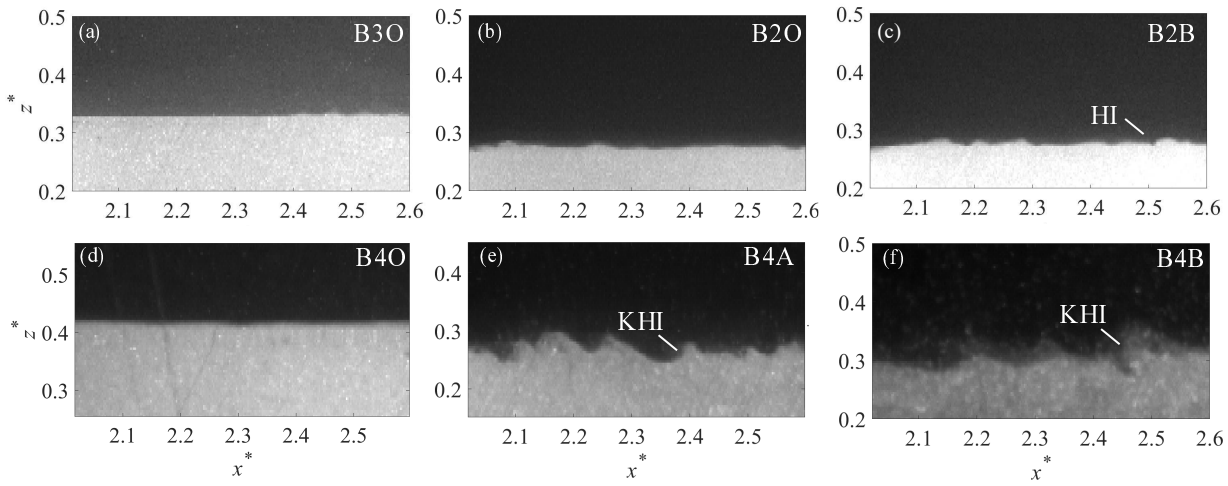

FIG. 12. Images of dye visualization for experiments (a) B3O with $Ri = 0.64$, (b) B2O with $Ri = 0.80$, (c) B2B with $Ri = 0.20$, (d) B4O with $Ri = 0.87$, (e) B4A with $Ri = 0.55$ and (f) B4B with $Ri = 0.35$.

This instability is characterized by two sets of waves, one set cusping into the upper layer and the second into the lower layer. Holmboe (1962) found that instabilities could occur for any positive bulk Richardson number, defined as:

$$Ri = g'\delta/(\Delta U)^2 \tag{6}$$

In the present study, *Ri* values have been evaluated by ADV velocity measurements, which were employed to perform simultaneous measurements to density profiles (values are given in Table I). Hazel (1972) extended the latter analysis and demonstrated that HI appear when $\delta/\eta > 2$, while KHI can occur when $\delta/\eta > 2$, only when $Ri < 0.07$. As such, smaller values of *Ri* favour the formation of KHI, with higher *Ri* favouring HI. When $\delta/\eta < 2$, the HI mode is suppressed (Smyth and Peltier, 1989) and therefore KHI can occur depending on the stratification and velocity shear profiles.

The two instabilities modes, HI and KHI, were observed during the experiments. In particular, the dye visualization of the experiments B3O, B2O, B2B, B4O, B4A and B4B are shown in Fig.12. In the uni-directional exchange flow run B3O with $f = 0.1$ rad $\cdot$ s^{-1} and $Ri = 0.64$, in Fig.12a, a stably stratified interface is shown, indicating no presence of instability. This is further observed also in run B4O (Fig.12d), with the largest rotation $f = 0.2$ rad $\cdot$ s^{-1}, indicating that the rotation acts to suppress the shear-driven interfacial instabilities such as KHI and HI. In fact, some interface perturbations are found in the uni-directional exchange flow experiment B2O, with a lower $f = 0.06$ rad $\cdot$ s^{-1}, exhibiting features of HI (Fig.12b). For the same $f = 0.06$ rad $\cdot$ s^{-1}, in

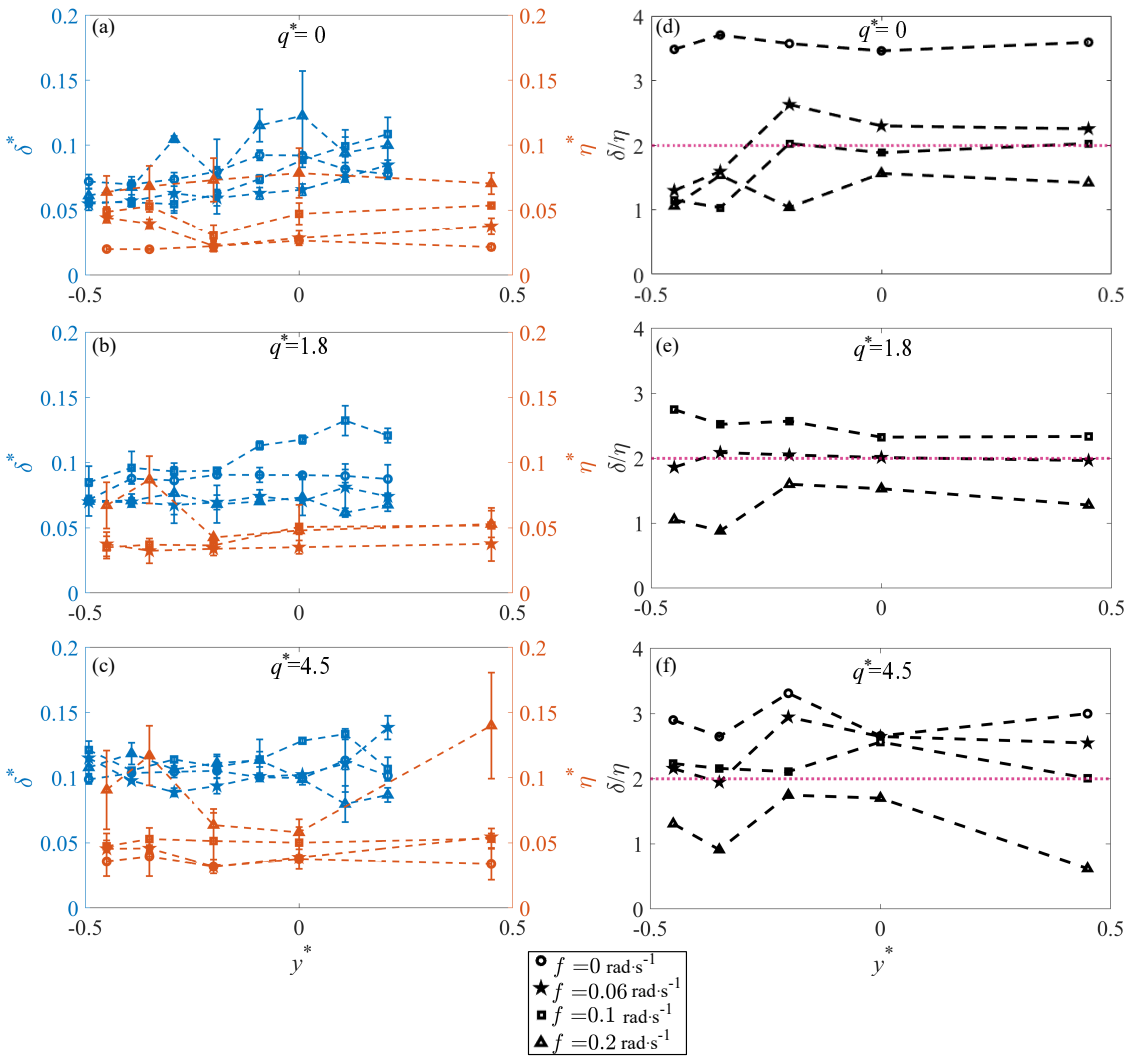

FIG. 13. Shear layer thickness δ^* and density layer thickness η^* for different f and (a) $q^* = 0$, (b) $q^* = 1.8$ and (c) $q^* = 4.5$. The corresponding δ/η is shown in (d), (e) and (f) respectively. Red dotted line marks the threshold condition for the formation of HI, i.e. $\delta/\eta = 2$.

the corresponding bi-directional exchange flow run B2B with $q^* = 4.5$ (Fig.12c), the increase in counter-flowing velocities in the upper and lower layer and thus δ, reflects in the formation of HI with two oppositely propagating modes, demonstrating that the velocity difference across the interface has a major role in governing the mode of instability. For a larger Coriolis parameter $f = 0.2$ rad $\cdot$ s^{-1} in the bi-directional exchange flow runs B4A and B4B, the transition to KHI is observed, with billows developing at the interface (Fig.12e-f), causing a largely mixed region, as observed in Part. III B from density profiles (see Fig.9b). Thus, in run B4O with $Bu = 0.43$, rotation suppresses interfacial instabilities, although as previously discussed an unsteady dense

outflow is largely influenced by baroclinic instability. The increasing net-barotropic conditions in run B4A and B4B with $Bu = 0.38$ and 0.3 respectively, which are also characterized by a baroclinic instability, induce favorable conditions of shear at the interface, for the formation of KHI billows that are responsible for entrainment and turbulent mixing at the interface in the stratified exchange flows.

This is further investigated in Fig.13, where both normalized $\delta^* = \delta/H_{ch}$ and $\eta^* = \eta/H_{ch}$ are displayed for varying f and q^*. Specifically, the evaluated δ^* has been averaged between three x locations in the PIV domain ($x =$ 260, 280 and 300 cm), while η^* between the three measurements locations D, E and F. The error-bars in Fig.13a-c, represent the standard deviation between measurements. A general increase of the shear layer thickness δ^* is found for increasing q^* in Fig.13a-c, from $\delta^* \simeq$ 0.058-0.068 for $q^* = 0$ (Fig.13a), to $\delta^* \simeq$ 0.062-0.092 for $q^* = 1.8$ (Fig.13b) and $\delta^* \simeq$ 0.092-0.114 for $q^* = 4.5$ (Fig.13c), while the effect of rotation appears to be negligible. Furthermore, the density layer thickness η^* is shown to be influenced by both f and q^*. In fact, η^* increases for larger f, in both uni-directional exchange flows with $\eta^* = 0.02$ for $f = 0$ up to $\eta^* =$ 0.08-0.11 for $f = 0.2$ rad $\cdot$ s^{-1} (Fig.13a) and bi-directional exchange flows with $q^* = 4.5$ and $\eta^* = 0.04$ for $f = 0$ up to $\eta^* =$ 0.09-0.16 for $f = 0.2$ rad $\cdot$ s^{-1} (Fig.13c). The associated δ/η values are shown in Fig.13d-f for the different f and q^* conditions tested. Specifically, when $q^* = 0$ in the non rotating experiment B1O and rotating experiment B2O ($f = 0.06$ rad $\cdot$ s^{-1}), $Ri \simeq 0.80$ and $\delta/\eta > 2$, indicating the formation of HI (Fig.13d). However, for $f > 0$ and $q^* = 0$, $\delta/\eta < 2$ for runs B3O and B4O, confirming that rotation acts to suppress HI (Fig.13d). In these experiments the computed $Ri \simeq 0.64 - 0.88$, for which the formation of KHI is also not possible, thus a stable interface is found (see Fig.12a). Further, for $q^* > 0$ (Fig.13e-f), $\delta/\eta \simeq 2$ for run B2A and $\delta/\eta > 2$ for runs B3A,B2B and B3B, indicating that the net-barotropic forcing in the fresh upper layer contributes to the formation of HI. By contrast, for the highest rotation rate tested ($f = 0.2$ rad $\cdot$ s^{-1}), $\delta/\eta < 2$ for all the q^* tested. In particular, for $f = 0.2$ rad $\cdot$ s^{-1} and $q^* = 1.8$ and 4.5 (Fig.13e-f) the computed Ri lowers to $Ri = 0.55$ and $Ri = 0.35$ respectively, which make possible the transition to KHI (Fig.12e-f).

E. Fresh and saline water fluxes through trapezoidal channel

The fresh and saline water volume fluxes Q_F and Q_S through the right hand half of the trapezoidal channel ($y^* < 0$ where PIV measurements were acquired) can be evaluated as the sum of

the local volume fluxes q_{Si} and q_{Fi}, obtained as integration of each PIV velocity profiles measured in half of the channel (i.e. S1 $\rightarrow$ S9) as:

$$q_{Si} = \int_0^{h_{2i}} u_i W_i dz \tag{7}$$

$$q_{Fi} = \int_{h_{2i}}^{H_{ch}} u_i W_i dz \tag{8}$$

where h_{2i} is defined for each PIV section as in Part III A and W_i is the corresponding width of contribution, $W_i = 10$ cm for S2-8 and $W_i = 5$ cm for S1 and S9.

In Table II, the derived values of the relative magnitude of the counter-flowing water masses $Q^* = Q_F/Q_S$ and the individual saline and fresh layer flux ratios Q_s/Q_2 and Q_F/Q_1, are summarized. In Fig.14a and d, Q^* is plotted against the source volume flux ratio q^* and Burger number Bu, respectively. The green dashed line in Fig.14a and red lines in Fig.14d represent the $Q^* = q^*$ condition. In Fig.14a,d, the measured Q^* agrees reasonably well with the expected q^* value, especially for $Bu > 0.7$, with percentage difference less than 8% in most of the experiments conducted and 31% and 22% for runs B2A and B3B respectively. For the run at $q^* = 1.8$ and $f = 0.2$ rad$\cdot$s^{-1} (run B4A with $Bu = 0.38$, Table II), the volume flux ratio in the channel $Q^* < q^*$ with a percentage difference of 42%, possibly suggesting that the local fresh water volume flux Q_F is lower than imposed at the channel boundaries, due to interfacial mixing and entrainment/detrainment between the two layers, induced by KHI, as discussed in Part III D (see Figs.13e,12c). Furthermore, at $q^* = 4.5$ and $f \geq 0.1$ rad$\cdot$s^{-1}, in-channel flux ratio $Q^* > q^*$, with percentage difference of 193%, indicating that the upper fresh volume flux Q_F becomes dominant and the saline water intrusion flow is, to some extent, blocked (i.e. $Q_S < Q_2$) under the large net-barotropic condition and at higher rotation rates (as apparent from Fig.6c,d). This is in agreement with the observed ageostrophic motion previously discussed and reduced velocity u_2 in the lower layer.

This is further investigated in Fig.14b-c,e-f, in which the individual saline and fresh layer flux ratios Q_S/Q_2 and Q_F/Q_1 are plotted versus q^* and Bu. The general effect of the increasing rotation f and net-barotropic flow condition q^* is an overall reduction of the saline water outflow flux ratio Q_S/Q_2 through the trapezoidal channel, indicating that an increasing fraction of the saline water input into basin B is blocked by the combined effect of strong barotropic forcing in the upper layer and higher rotation rates. In fact, for a fixed f and Bu in Fig.14e, the increase in q^* causes the reduction of Q_S/Q_2, indicating again that the net-barotropic flow condition is a relevant parameter governing the dynamics of the outflowing dense layer. At $q^* = 1.8$, the channel saline flux ratio $Q_S/Q_2 = 0.38 - 0.42$, indicating a flux reduction of between 8 and 12% in half of the

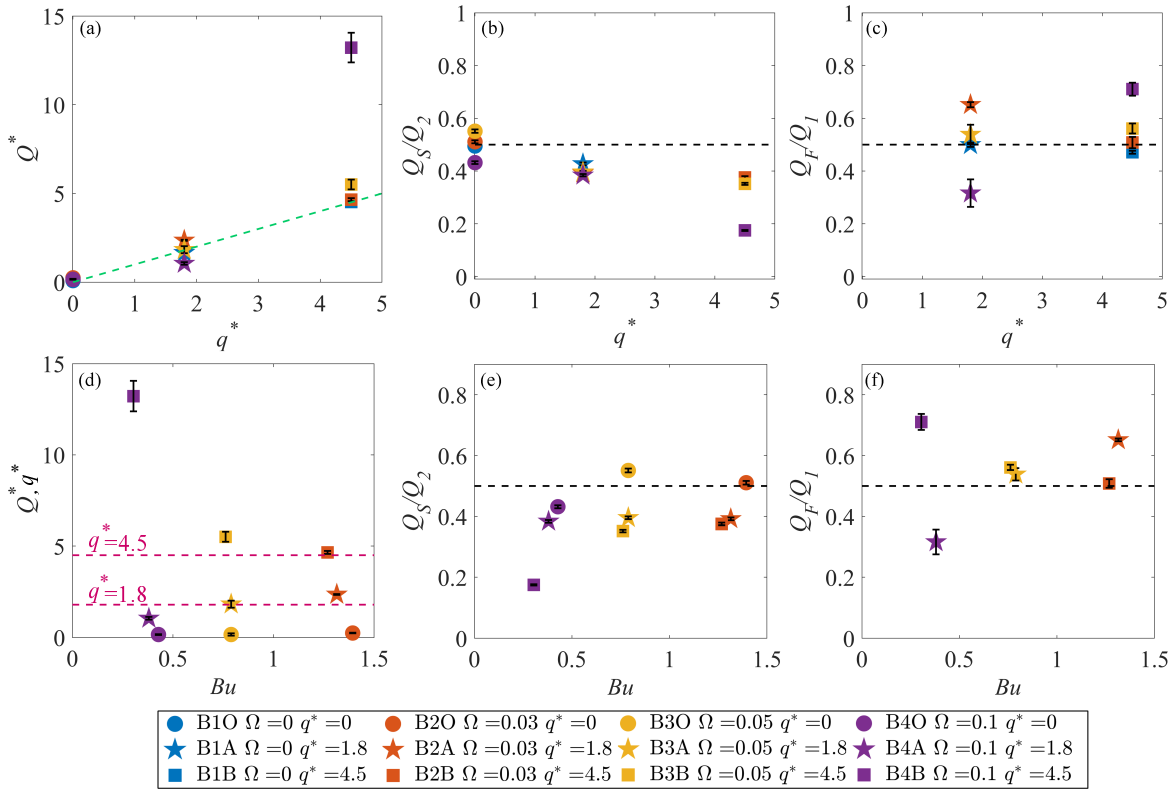

FIG. 14. Local ratio of fresh and saline water fluxes Q_F/Q_S passing through half of the channel plotted versus (a) imposed volume flux q^* at the channel boundary and (d) Bu. The green dashed line represents the condition $Q^* = q^*$, while the dashed red lines mark the $Q^* = 1.8$ and $Q^* = 4.5$. Non-dimensional saline volume fluxes ratio Q_S/Q_2 and Q_F/Q_1, versus (b,c) inflow volume flux ratio q^* and (e,f) Bu numbers. Black dashed lines represents $Q_{F,S}/Q_{1,2} = 0.5$. The errorbars show the confidence level of along-channel velocities $u_i(x,z)$

.

channel (TableII). By contrast, at $q^* = 4.5$, the channel saline flux ratio $Q_S/Q_2 = 0.17 - 0.37$, indicating that up to 33% of the saline input is blocked at the the highest q^* and rotation condition (i.e. $f = 0.2$ rad $\cdot$ s^{-1} and $Bu = 0.3$), in the half of the channel considered. This flux reduction is particularly significant as geostrophic adjustment of the dense outflow layer means that the vast majority of the remaining dense water flux passes through the half of the trapezoidal channel ($y^* < 0$) under consideration (see Fig.6c,d). Indeed, this suggests that the actual blockage of the saline outflow through the channel can be up to 66% of the inflow flux Q_2. It is also interesting to note that the equivalent reduction for the non-rotating ($f = 0$ rad $\cdot$ s^{-1}) case, with $q^* = 4.5$, is

TABLE II. Summary of derived fresh and saline water fluxes

Run	Bu	q^*	Q^*	Q_S/Q_2	Q_F/Q_1
B1O	–	0	0	0.5	–
B1A	–	1.8	1.66	0.43	0.5
B1B	–	4.5	4.52	0.37	0.47
B2O	1.39	0	0.24	0.51	–
B2A	1.31	1.8	2.36	0.39	0.65
B2B	1.27	4.5	4.65	0.37	0.51
B3O	0.79	0	0.16	0.55	–
B3A	0.79	1.8	1.83	0.39	0.54
B3B	0.76	4.5	5.5	0.35	0.56
B4O	0.43	0	0.16	0.43	–
B4A	0.38	1.8	1.05	0.38	0.32
B4B	0.30	4.5	13.22	0.17	0.71

13%, indicating that the combined high rotation rate and large upper fresh water flow conditions combine to provide the most effective blocking mechanism for the saline water outflow through the trapezoidal channel. In Fig.14c,f, the fresh layer flux ratio $Q_F/Q_1 \simeq 0.47-0.56$, in most of the experiments conducted. For the run at $q^* = 1.8$ and $f = 0.2$ rad $\cdot$ s^{-1}, however, the local fresh water volume flux Q_F is significantly lower than expected from the imposed inflow flux Q_1 at the channel boundary (i.e. $Q_F/Q_1 \simeq 0.32$). This is most probably again due to interfacial mixing and entrainment/detrainment between the two layers and KHI generated, as discussed in Sec.III D. Furthermore, at $q^* = 4.5$ and $f = 0.2$ rad $\cdot$ s^{-1}, i.e. run B4B, $Q_F/Q_1 = 0.71$, confirming that the upper fresh volume flux Q_F becomes dominant on the dynamic of the exchange flow.

This finding has clear implications for determining the relative parametric influence of Coriolis forces and net-barotropic forcing on the dynamics and control of stratified exchange flows through sea straits and deep ocean passages.

Indeed, for the Bornholm and Irbe Straits in the Baltic Sea, predictions of the controlled transport through these passages were obtained by 1 1/2-layer rotating hydraulic simulations (Laanearu and Lundberg, 2003) that were approximately 43% and 38% higher than the measured or observationally determined baroclinic transport of 100,000 m$^3 \cdot$ s^{-1} (Liljebladh and Stigebrandt, 1996) and

5,200 $m^3 \cdot s^{-1}$ (Lilover et al., 1998), respectively. These discrepancies were associated with model assumptions of (a) topographic conditions (i.e. variations of channel cross-section from the idealised parabolic shape modelled), (b) inviscid flow conditions (i.e. frictional effects negligible), (c) a passive upper layer (i.e. no fluid motion in surface layer, e.g. from freshwater fluxes), and (d) the assumption of stationary flow (i.e. barotropic outflows associated with tidal and/or wind forcing neglected). These model assumptions were only deemed to be marginally satisfied within the two straits, with spatio-temporal variations in local conditions thought to result in the potential restriction or blockage of deep-water flows through these straits.

IV. CONCLUSIONS

In this paper, a novel large-scale experimental study on bottom uni and bi-directional exchange flows propagating along a rotating, trapezoidal-shaped channel, is presented. The experiments were targeted at obtaining detailed synoptic velocity fields for these flows from PIV measurements across the flume, as well as density profiles measured at specific transverse locations by micro-conductivity probes. Under non-rotating conditions, the velocity fields highlight the role of the upper fresh water flow in reducting the dense layer thickness h_2, which is also accompanied by an increase of the shear layer thickness induced by as the relative magnitude of fresh and saline inflow q^* increases. In agreement with previous studies, the Bu is the main governing non-dimensional parameter characterizing the dynamics of stratified rotating exchange flows. In the present study, for $Bu > 0.7$ the Coriolis acceleration imposed by the channel rotation causes the geostrophic adjustment of the outflowing dense saline layer to the right hand channel side wall. In this case, the cross-channel inclination of the current depth defined by the zero-velocity interface, increases with both f and q^*, and consequently a cross-channel variation of the along-channel velocity component in the lower layer u_2 is found, with velocity increasing from the channel side to the center line. The effect of rotation on the transverse dense layer distribution is also enhanced by the net-barotropic flow conditions, causing the reduction of u_2 in the lower layer and the increase of the upper fresh flow velocity u_1 on the side wall of the trapezoidal-shaped channel. By contrast, for $Bu < 0.5$, the exchange flows are characterized by time and space variability and baroclinic instability in the outflowing dense layer. In particular for the largest Coriolis parameter $f = 0.2$ rad $\cdot s^{-1}$ and net-barotropic flow condition $q^* = 4.5$, the outflowing saline water layer is strongly deflected to the right hand side of the channel and the corresponding u_2 and h_2 are reduced sig-

nificantly, indicating that the intrusion is also partially blocked by the dominant upper fresh water flow. Moreover, in the bi-directional runs with $Bu < 0.5$, the interface slope of the dense outflowing layer deviates from the evaluated geostrophic slopes indicating the presence of ageostrophic motion, due to the baroclinic instability. This is further confirmed by evaluation of the local water fluxes Q_F and Q_S through half of the trapezoidal channel, which are obtained from integrating the along-channel velocity profiles measured at transverse sections across the flume. In particular the fraction of fresh and saline water fluxes $Q^* = q^*$ for most of the experiments performed, except run B4A for which $Q^* < q^*$ and run B3B and B4B, in which case $Q^* > q^*$. In this latter particular condition of f and q^*, $Q_S/Q_2 \simeq 0.17$, indicating that only the 17% of the intrusion is flowing within half of the channel and a partial blockage occurred. In general, the dimensionless saline water flux Q_S/Q_2 is observed to decrease with both f and q^*.

The analysis of dimensionless density profiles, confirmed the role of the two dominant mechanism on the transverse distribution of isopycnals elevation. The upper fresh water flow causes the reduction of the $\rho^* = 0.5$ isopycnal elevation and the increase of the mixing layer thickness. Whereas the increase of f induces an overall increase in $z^*_{\rho^*=0.5}$, which is larger on the lateral side wall of the channel. In the rotating stratified exchange flow, the two parametric conditions, f and q^* play a key role, depending on which of the two dominates the dynamics of the counter-flowing water masses. The resulting coupled effect of q^* and f, is the increase of the $\rho^* = 0.5$ isopycnal elevation slope, with the complete reduction of the dense layer in the left side of the channel, in agreement with the velocity measurements. A general increase of the mixing layer thickness is found with both q^* and f. In fact, shear-driven interfacial instabilities such as HI and KHI, are suppressed for uni-directional exchange flows with $f > 0$, for which $\delta/\eta < 2$. By contrast, for bi-directional exchange flows, q^* plays a key role in the formation of both HI and KHI depending on the stratification and shear velocity at the interface. HI are observed for $q^* > 0$ and $f = 0.06$, while for the highest Coriolis parameter $f = 0.1$ rad $\cdot$ s^{-1} and $q^* = 1.8$ and 4.5, the transition to KHI is reached, which contributed to the enanched mixing and entrainment of the outflowing dense current. It can be concluded that in general, turbulent mixing due to velocity shear near the density interface was responsible for the interfacial instabilities such as Kelvin-Helmholtz billows or Holmboe waves, and the background vorticity due to rotation was responsible for the geostrophic adjustment of stratified flow in the trapezoidal channel.

In conclusion the present study, provide insight in the complex dynamics of uni and bi-directional exchange flows and the significant influence of the net-barotropic forcing, coupled with Coriolis

effects, on the lateral distribution of the counter-flowing water masses.

ACKNOWLEDGEMENTS

This project has received funding from the European Union's Horizon 2020 research and innovation programme under grant agreement No 654110, HYDRALAB+. This research was also funded by the Italian Ministry of Education, University and Research (MIUR) through the Departments of Excellence 2018-2022 Program. We thank Katrin Kaur, Samuel Viboud e Thomas Valran for providing invaluable discussion and able assistance to carry out the laboratory experiments.

DATA AVAILABILITY

The data that support the findings of this study are available from the corresponding author upon reasonable request.

REFERENCES

O. Andrejev, K. Myrberg, P. Alenius, and P. A. Lundberg. Mean circulation and water exchange in the gulf of Finland-a study based on three-dimensional modelling. *Boreal Environment Research*, 9(1):1–16, 2004.

L. Arneborg, V. Fiekas, L. Umlauf, and H. Burchard. Gravity current dynamics and entrainment—a process study based on observations in the Arkona Basin. *Journal of Physical Oceanography*, 37(8):2094–2113, 2007.

S. Balasubramanian and Q. Zhong. Entrainment and mixing in lock-exchange gravity currents using simultaneous velocity-density measurements. *Physics of Fluids*, 30(5):056601, 2018.

J. Berntsen, E. Darelius, and H. Avlesen. Gravity currents down canyons: effects of rotation. *Ocean Dynamics*, 66(10):1353–1378, 2016.

R. K. Bhagat, M. S. D. Wykes, S. B. Dalziel, and P. F. Linden. Effects of ventilation on the indoor spread of COVID-19. *Journal of Fluid Mechanics*, 903, 2020.

K. Borenäs and J. Whitehead. Upstream separation in a rotating channel flow. *Journal of Geophysical Research: Oceans*, 103(C4):7567–7578, 1998.

C. Caulfield. Layering, instabilities, and mixing in turbulent stratified flows. *Annual Review of Fluid Mechanics*, 53, 2020.

C. Cenedese and C. Adduce. Mixing in a density-driven current flowing down a slope in a rotating fluid. *Journal of Fluid Mechanics*, 604:369–388, 2008.

C. Cenedese and C. Adduce. A new parameterization for entrainment in overflows. *Journal of Physical Oceanography*, 40:1835–1850, 2010.

C. Cenedese, J. A. Whitehead, T. Ascarelli, and M. Ohiwa. A dense current flowing down a sloping bottom in a rotating fluid. *Journal of Physical Oceanography*, 34(1):188–203, 2004.

R. Cossu and M. G. Wells. Coriolis forces influence the secondary circulation of gravity currents flowing in large-scale sinuous submarine channel systems. *Geophysical Research Letters*, 37 (17), 2010.

R. Cossu and M. G. Wells. The evolution of submarine channels under the influence of Coriolis forces: experimental observations of flow structures. *Terra Nova*, 25(1):65–71, 2013.

R. Cossu, M. G. Wells, and A. Wåhlin. Influence of the Coriolis force on the velocity structure of gravity currents in straight submarine channel systems. *Journal of Geophysical Research: Oceans*, 115(C11), 2010.

B. Cushman-Roisin and J.-M. Beckers. *Introduction to geophysical fluid dynamics: physical and numerical aspects*. Academic press, 2011.

A. Cuthbertson, P. Lundberg, P. Davies, and J. Laanearu. Gravity currents in rotating, wedge-shaped, adverse channels. *Environmental Fluid Mechanics*, 14(5):1251–1273, 2014.

A. Cuthbertson, J. Laanearu, M. Carr, J. Sommeria, and S. Viboud. Blockage of saline intrusions in restricted, two-layer exchange flows across a submerged sill obstruction. *Environmental Fluid Mechanics*, 18(1):27–57, 2018.

A. Cuthbertson, J. Berntsen, J. Laanearu, and M. Asplin. Rotational effects on exchange flows across a submerged sill. *Environmental Fluid Mechanics*, 2020. *submitted for publication*.

A. J. Cuthbertson, J. Laanearu, A. K. Wåhlin, and P. A. Davies. Experimental and analytical investigation of dense gravity currents in a rotating, up-sloping and converging channel. *Dynamics of Atmospheres and Oceans*, 52(3):386–409, 2011.

A. Dai and C. S. Wu. High-resolution simulations of cylindrical gravity currents in a rotating system. *Journal of Fluid Mechanics*, 806:71–101, 2016.

A. Dai and C. S. Wu. High-resolution simulations of unstable cylindrical gravity currents undergoing wandering and splitting motions in a rotating system. *Physics of Fluids*, 30(2):026601, 2018.

S. B. Dalziel and G. F. Lane-Serff. The hydraulics of doorway exchange flows. *Building and Environment*, 26(2):121–135, 1991.

E. Darelius. Topographic steering of dense overflows: Laboratory experiments with v-shaped ridges and canyons. *Deep Sea Research Part I: Oceanographic Research Papers*, 55(8):1021–1034, 2008.

S. Davarpanah Jazi, M. G. Wells, J. Peakall, R. M. Dorrell, R. E. Thomas, G. M. Keevil, S. E. Darby, J. Sommeria, S. Viboud, and T. Valran. Influence of Coriolis force upon bottom boundary layers in a large-scale gravity current experiment: Implications for evolution of sinuous deep-water channel systems. *Journal of Geophysical Research: Oceans*, 125(3):e2019JC015284, 2020.

P. Davies, A. Wåhlin, and Y. Guo. Laboratory and analytical model studies of the Faroe Bank Channel deep-water outflow. *Journal of Physical Oceanography*, 36(7):1348–1364, 2006.

M. C. De Falco, L. Ottolenghi, and C. Adduce. Dynamics of gravity currents flowing up a slope and implications for entrainment. *Journal of Hydraulic Engineering*, 146(4):04020011, 2020.

M. C. De Falco, C. Adduce, M. E. Negretti, and E. J. Hopfinger. On the dynamics of quasi-steady gravity currents flowing up a slope. *Advances in Water Resources*, 147:103791, 2021.

D. Farmer and L. Armi. Stratified flow over topography: the role of small-scale entrainment and mixing in flow establishment. *Proceedings of the Royal Society of London. Series A: Mathematical, Physical and Engineering Sciences*, 455(1989):3221–3258, 1999.

I. Fer, G. Voet, K. S. Seim, B. Rudels, and K. Latarius. Intense mixing of the faroe bank channel overflow. *Geophysical Research Letters*, 37(2), 2010.

L. Filleul, S. Cassadou, S. Médina, P. Fabres, A. Lefranc, D. Eilstein, A. Le Tertre, L. Pascal, B. Chardon, M. Blanchard, et al. The relation between temperature, ozone, and mortality in nine french cities during the heat wave of 2003. *Environmental Health Perspectives*, 114(9): 1344–1347, 2006.

H. Fouli and D. Z. Zhu. Interfacial waves in two-layer exchange flows downslope of a bottom sill. *Journal of Fluid Mechanics*, 680:194, 2011.

A. E. Gill. Atmosphere-ocean dynamics. 30:662, 1982.

J. B. Girton, L. J. Pratt, D. A. Sutherland, and J. F. Price. Is the Faroe Bank Channel overflow hydraulically controlled? *Journal of Physical Oceanography*, 36(12):2340–2349, 2006.

M. Gregg, E. D'Asaro, J. Riley, and E. Kunze. Mixing efficiency in the ocean. *Annual review of marine science*, 10:443–473, 2018.

R. Griffiths. Gravity currents in rotating systems. *Annual Review of Fluid Mechanics*, 18(1): 59–89, 1986.

P. Hazel. Numerical studies of the stability of inviscid stratified shear flows. *Journal of Fluid Mechanics*, 51(1):39–61, 1972.

J. Holmboe. On the behavior of symmetric waves in stratified shear layers. *Geophysics Publications*, 24:67–113, 1962.

R. Inghilesi, C. Adduce, V. Lombardi, F. Roman, and V. Armenio. Axisymmetric three-dimensional gravity currents generated by lock exchange. *Journal of Fluid Mechanics*, 851: 507–544, 2018.

G. C. Johnson and D. R. Ohlsen. Frictionally modified rotating hydraulic channel exchange and ocean outflows. *Journal of Physical Oceanography*, 24(1):66–78, 1994.

T. Kóuts and A. Omstedt. Deep water exchange in the Baltic Proper. *Tellus A: Dynamic Meteorology and Oceanography*, 45(4):311–324, 1993.

G. La Forgia, L. Ottolenghi, C. Adduce, and F. Falcini. Intrusions and solitons: Propagation and collision dynamics. *Physics of Fluids*, 32(7):076605, 2020.

M. La Rocca, P. Prestininzi, C. Adduce, G. Sciortino, R. Hinkelmann, et al. Lattice boltzmann simulation of 3D gravity currents around obstacles. *International Journal Offshore Polar Engineering*, 23(03), 2013.

J. Laanearu and P. Lundberg. Topographically constrained deep-water flows in the Baltic Sea. *Journal of Sea Research*, 49(4):257–265, 2003.

J. Laanearu, U. Lips, and P. Lundberg. On the application of hydraulic theory to the deep-water flow through the Irbe Strait. *Journal of Marine Systems*, 25(3-4):323–332, 2000.

J. Laanearu, A. J. Cuthbertson, and P. A. Davies. Dynamics of dense gravity currents and mixing in an up-sloping and converging vee-shaped channel. *Journal of Hydraulic Research*, 52(1): 67–80, 2014.

A. Lefauve and P. F. Linden. Buoyancy-driven exchange flows in inclined ducts. *Journal of Fluid Mechanics*, 893:A2, 2020.

B. Liljebladh and A. Stigebrandt. Observations of the deepwater flow into the Baltic Sea. *Journal of Geophysical Research: Oceans*, 101(C4):8895–8911, 1996.

M. J. Lilover, U. Lips, J. Laanearu, and B. Liljebladh. Flow regime in the Irbe Strait. *Aquatic sciences*, 60(3):253–265, 1998.

P. F. Linden. The fluid mechanics of natural ventilation. *Annual Review of Fluid Mechanics*, 31 (1):201–238, 1999.

P. F. Linden and G. J. F. V. Heijst. Two-layer spin-up and frontogenesis. *Journal of Fluid Mechanics*, 143:69–94, 1984. doi:10.1017/S0022112084001269.

V. Lombardi, C. Adduce, and M. La Rocca. Unconfined lock-exchange gravity currents with variable lock width: laboratory experiments and shallow-water simulations. *Journal of Hydraulic Research*, 56(3):399–411, 2018.

R. Lu and R. P. Turco. Air pollutant transport in a coastal environment. part i: Two-dimensional simulations of sea-breeze and mountain effects. *J. Atmos. Sci.*, 51(15):2285–2308, 1994.

P. MacCready, R. M. McCabe, S. A. Siedlecki, M. Lorenz, S. N. Giddings, J. Bos, S. Albertson, N. Banas, and S. Garnier. Estuarine circulation, mixing, and residence times in the Salish Sea. *Journal of Geophysical Research: Oceans*, page e2020JC016738, 2020.

J. Martin and G. Lane-Serff. Rotating gravity currents. part 1. energy loss theory. *Journal of Fluid Mechanics*, 522:35, 2005.

J. Martin, D. Smeed, and G. Lane-Serff. Rotating gravity currents. part 2. potential vorticity theory. *Journal of Fluid Mechanics*, 522:63, 2005.

W. Matthäus and H. Ulrich Lass. The recent salt inflow into the Baltic Sea. *Journal of Physical Oceanography*, 25(2):280–286, 1995.

T. Maxworthy. On turbulent mixing across a density interface in the presence of rotation. *Journal of Physical Oceanography*, 16(6):1136–1137, 1986.

N. Mingotti, R. Wood, C. Noakes, and A. W. Woods. The mixing of airborne contaminants by the repeated passage of people along a corridor. *Journal of Fluid Mechanics*, 903:A52, 2020. doi:10.1017/jfm.2020.671.

M. E. Negretti, D. Z. Zhu, and G. H. Jirka. Barotropically induced interfacial waves in two-layer exchange flows over a sill. *Journal of Fluid Mechanics*, 592:135, 2007.

M. E. Negretti, D. Z. Zhu, and G. H. Jirka. The effect of bottom roughness in two-layer flows down a slope. *Dynamics of Atmospheres and Oceans*, 45(1-2):46–68, 2008.

L. Ottolenghi, C. Adduce, R. Inghilesi, F. Roman, and V. Armenio. Mixing in lock-release gravity currents propagating up a slope. *Physics of Fluids*, 28(5):056604, 2016.

L. Ottolenghi, C. Cenedese, and C. Adduce. Entrainment in a dense current flowing down a rough sloping bottom in a rotating fluid. *Journal of Physical Oceanography*, 47(3):485–498, 2017.

L. Ottolenghi, C. Adduce, F. Roman, and G. la Forgia. Large eddy simulations of solitons colliding with intrusions. *Physics of Fluids*, 32(9):096606, 2020.

B. Rabe, D. Smeed, S. Dalziel, and G. Lane-Serff. Experimental studies of rotating exchange flow. *Deep Sea Research Part I: Oceanographic Research Papers*, 54(2):269–291, 2007.

F. E. Sargent and G. H. Jirka. Experiments on saline wedge. *Journal of Hydraulic Engineering*, 113(10):1307–1323, 1987.

J. E. Simpson. *Sea breeze and local winds*. Cambridge University Press, 1994.

W. Smyth and W. Peltier. The transition between kelvin–helmholtz and holmboe instability: An investigation of the overreflection hypothesis. *Journal of the Atmospheric Sciences*, 46(24): 3698–3720, 1989.

L. Umlauf, L. Arneborg, R. Hofmeister, and H. Burchard. Entrainment in shallow rotating gravity currents: A modeling study. *Journal of Physical Oceanography*, 40(8):1819–1834, 2010.

M. Wells. Influence of Coriolis forces on turbidity currents and sediment deposition. In *Particle-laden flow*, pages 331–343. Springer, 2007.

M. Wells and R. Cossu. The possible role of coriolis forces in structuring large-scale sinuous patterns of submarine channel-levee systems. *Philosophical Transactions of the Royal Society A: Mathematical, Physical and Engineering Sciences*, 371(2004):20120366, 2013.

C.-S. Wu and A. Dai. Experiments on two-layer stratified gravity currents in the slumping phase. *Journal of Hydraulic Research*, 58(5):831–844, 2020.

D. Z. Zhu and G. A. Lawrence. Holmboe's instability in exchange flows. *Journal of Fluid Mechanics*, 429:391–409, 2001. doi:10.1017/S002211200000286X.

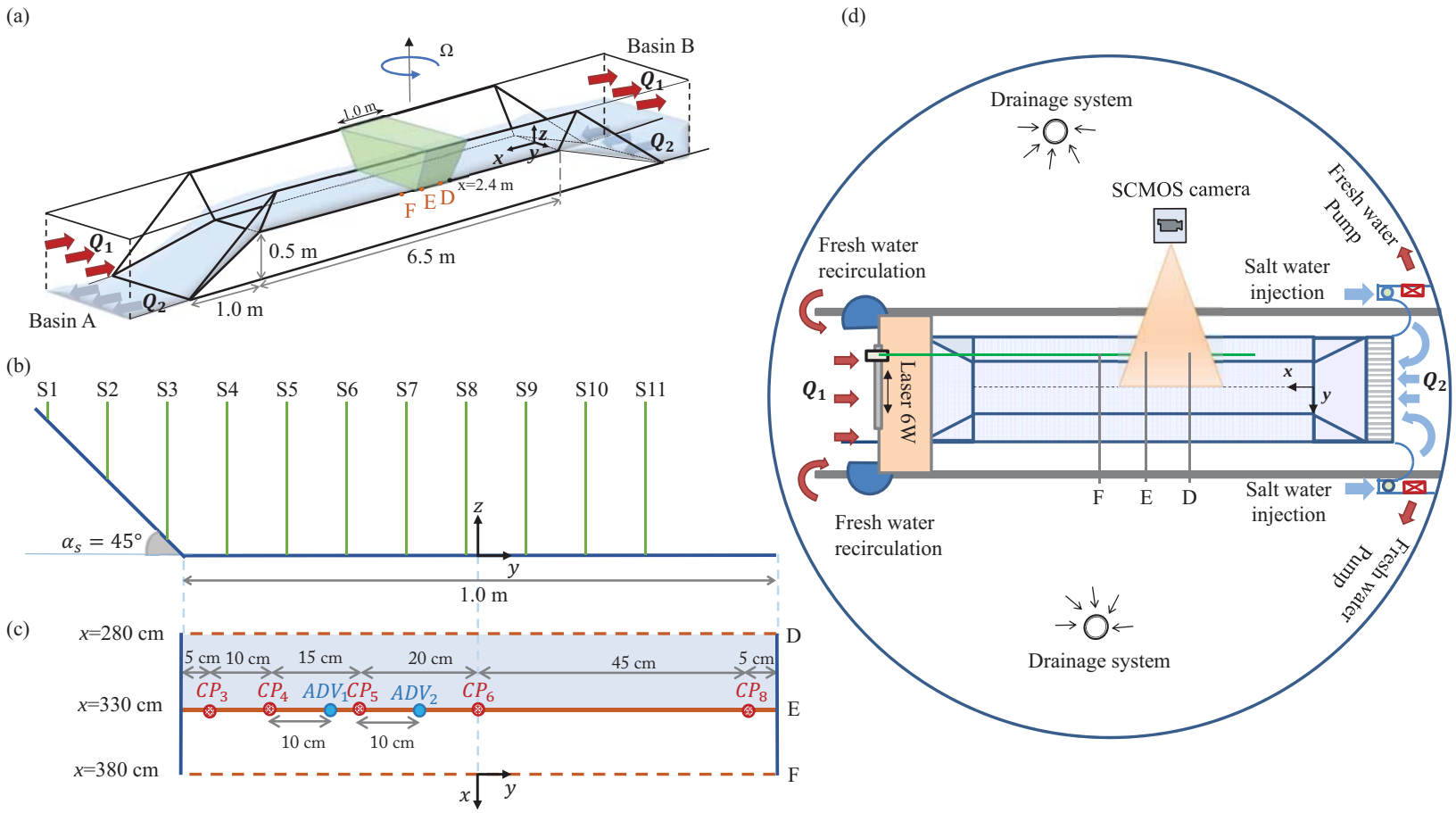
(a)
Ω
Basin B
Q_1
Q_2
1.0 m
z
x
y
x=2.4 m
F E D
Q_1
0.5 m
6.5 m
Q_2
1.0 m
Basin A
(b)
S1 S2 S3 S4 S5 S6 S7 S8 S9 S10 S11
$\alpha_s = 45°$
z
y
1.0 m
(c)
x=280 cm
x=330 cm
x=380 cm
5 cm 10 cm 15 cm 20 cm 45 cm 5 cm
CP_3 CP_4 ADV_1 CP_5 ADV_2 CP_6 CP_8
10 cm 10 cm
D E F
x y
(d)
Drainage system
SCMOS camera
Fresh water Pump
Fresh water recirculation
Salt water injection
Q_1
Laser 6W
x y
Q_2
F E D
Salt water injection
Fresh water recirculation
Fresh water Pump
Drainage system

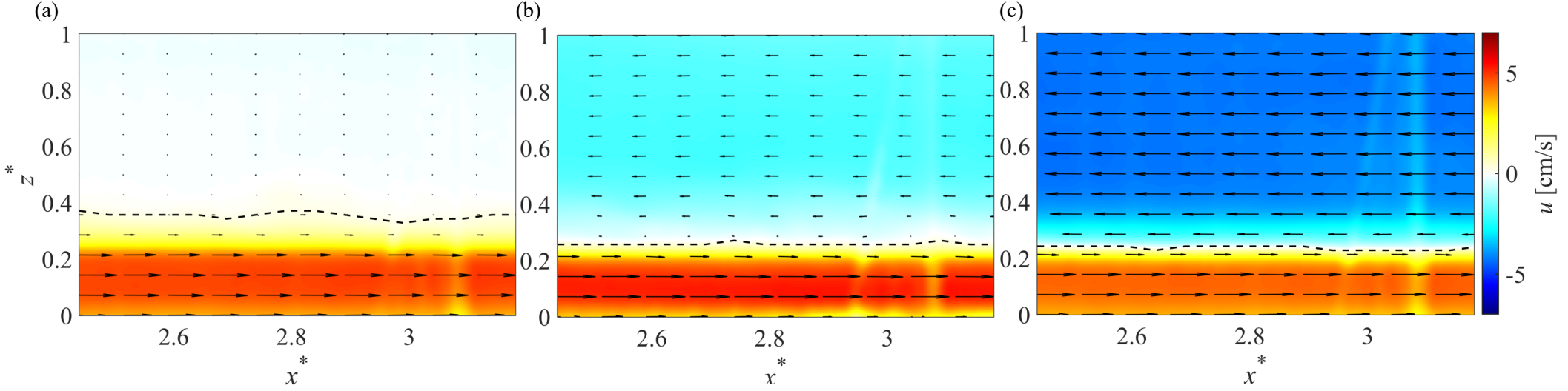
(a)
(b)
(c)
1
0.8
0.6
0.4
0.2
0
z^*
2.6
2.8
3
x^*
5
0
-5
u [cm/s]

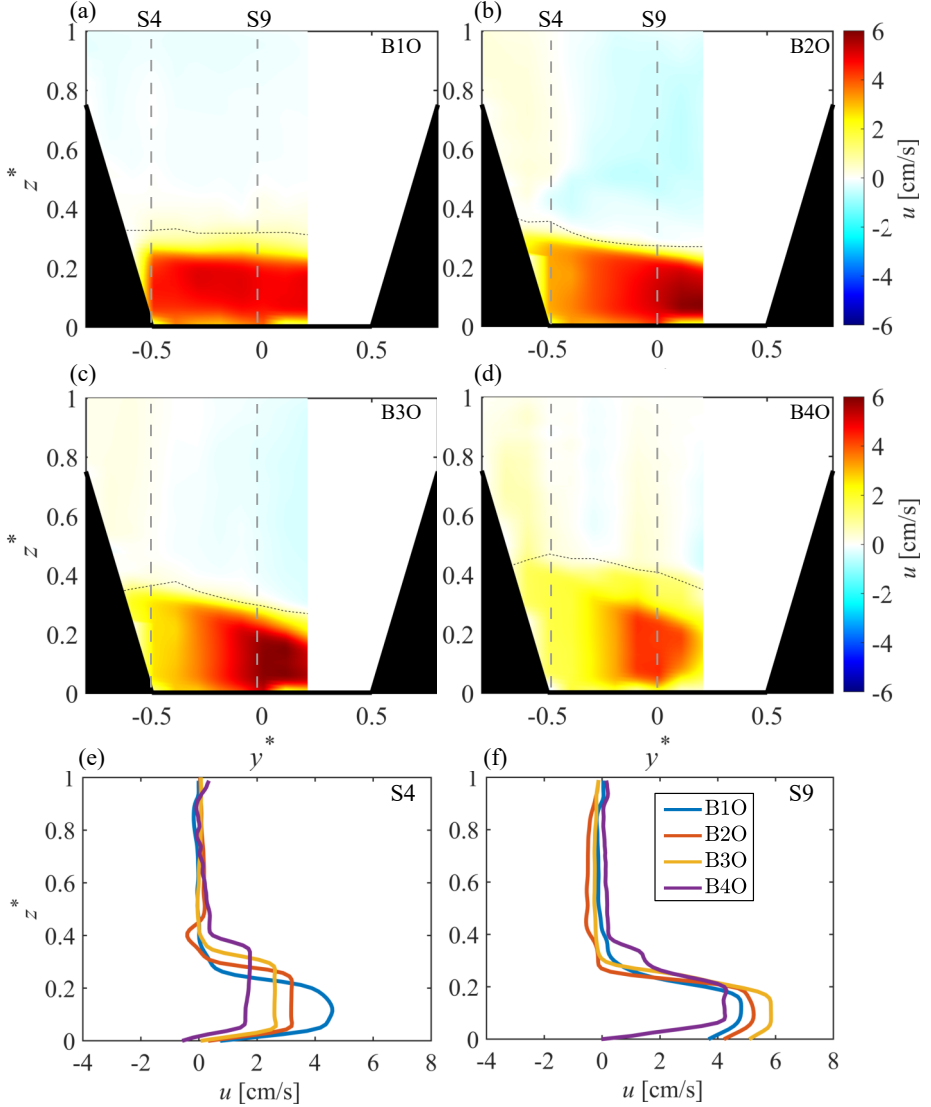
(a)
S4
S9
B1O
(b)
S4
S9
B2O
(c)
B3O
(d)
B4O
z*
y*
u [cm/s]
(e)
S4
(f)
S9
B1O
B2O
B3O
B4O
u [cm/s]

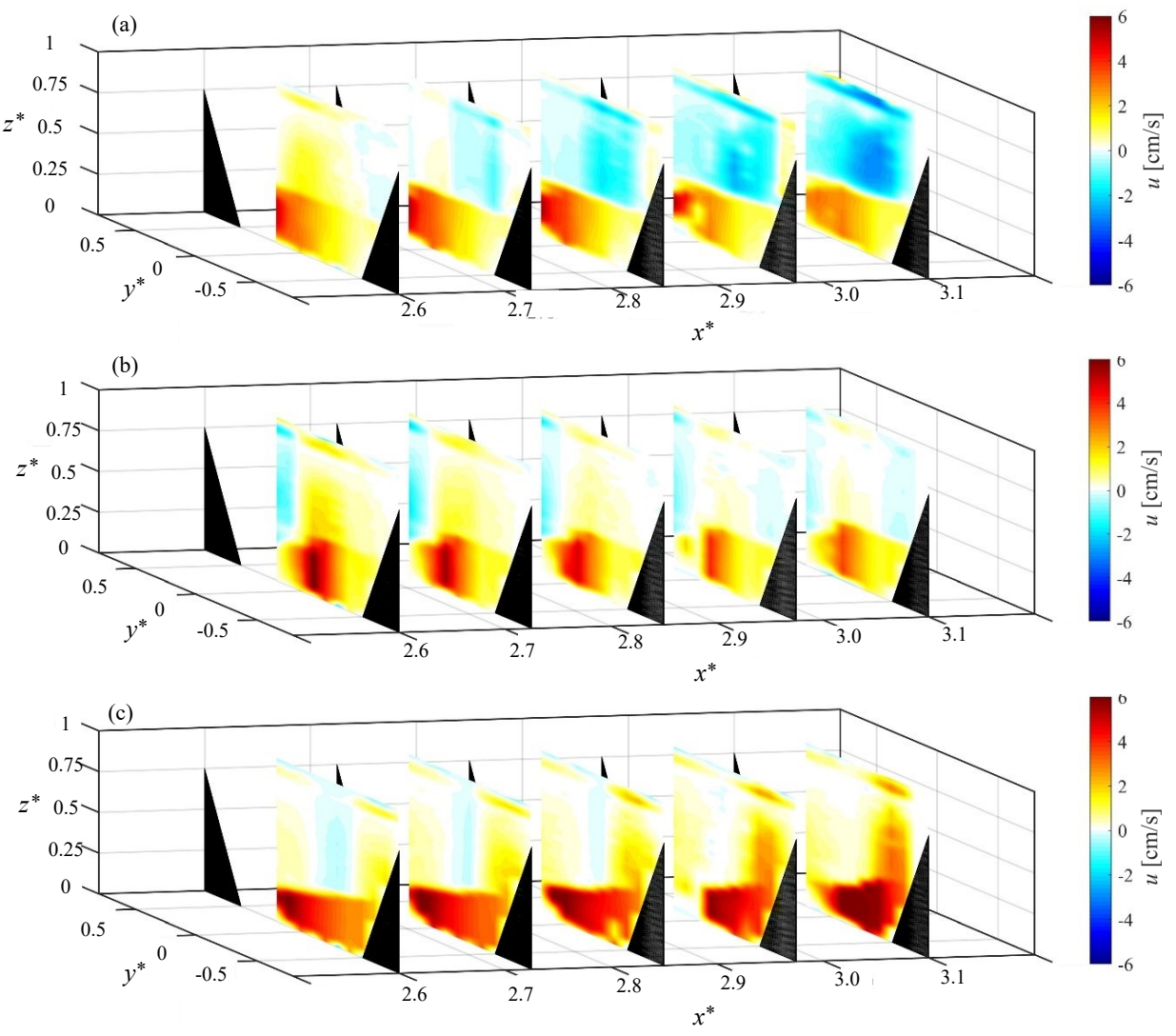
(a)
(b)
(c)
z*
y*
x*
u [cm/s]
1
0.75
0.5
0.25
0
0.5
0
-0.5
2.6
2.7
2.8
2.9
3.0
3.1
6
4
2
0
-2
-4
-6

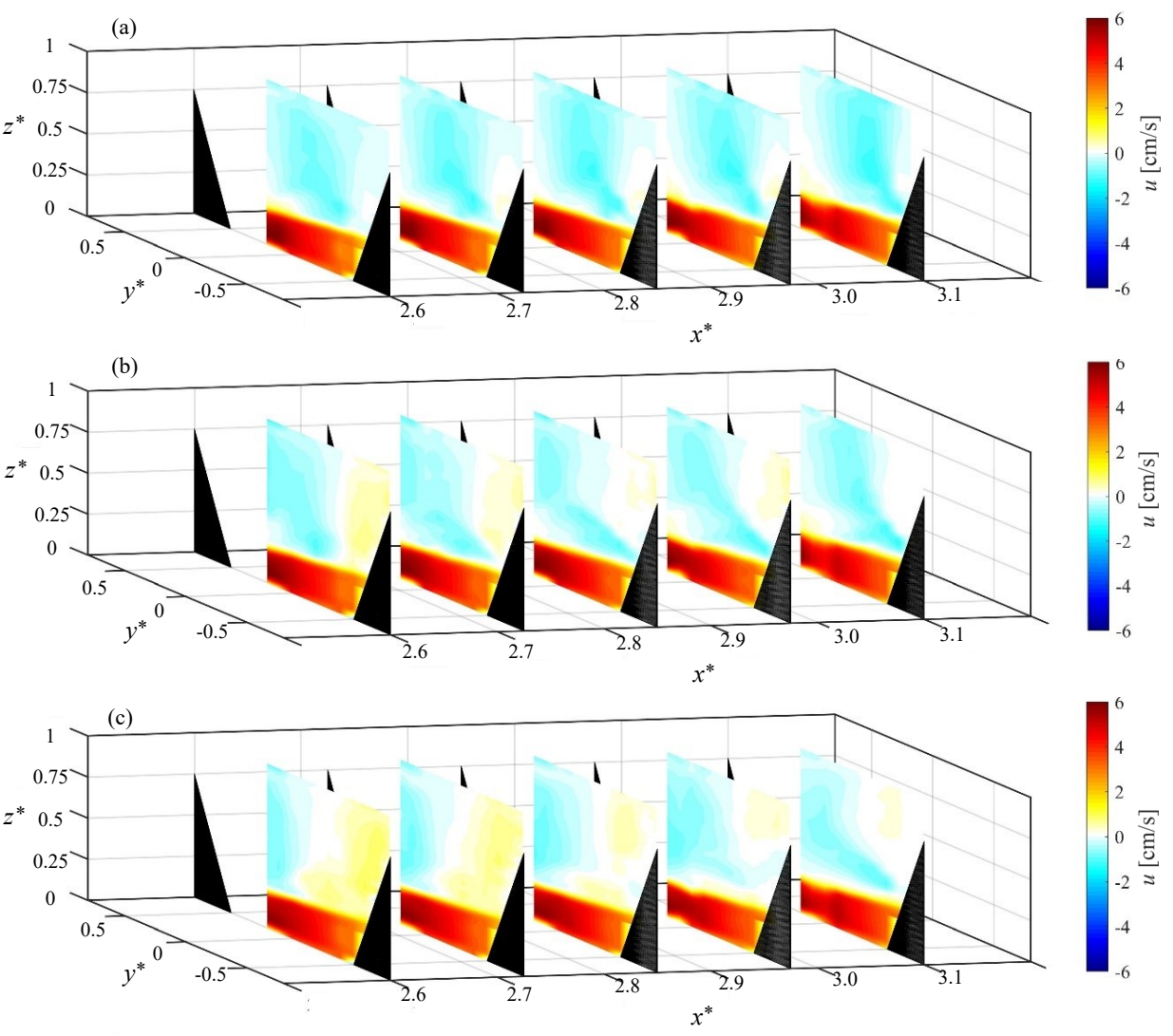
(a)
(b)
(c)
z^*
1
0.75
0.5
0.25
0
y^*
0.5
0
-0.5
x^*
2.6
2.7
2.8
2.9
3.0
3.1
u [cm/s]
6
4
2
0
-2
-4
-6

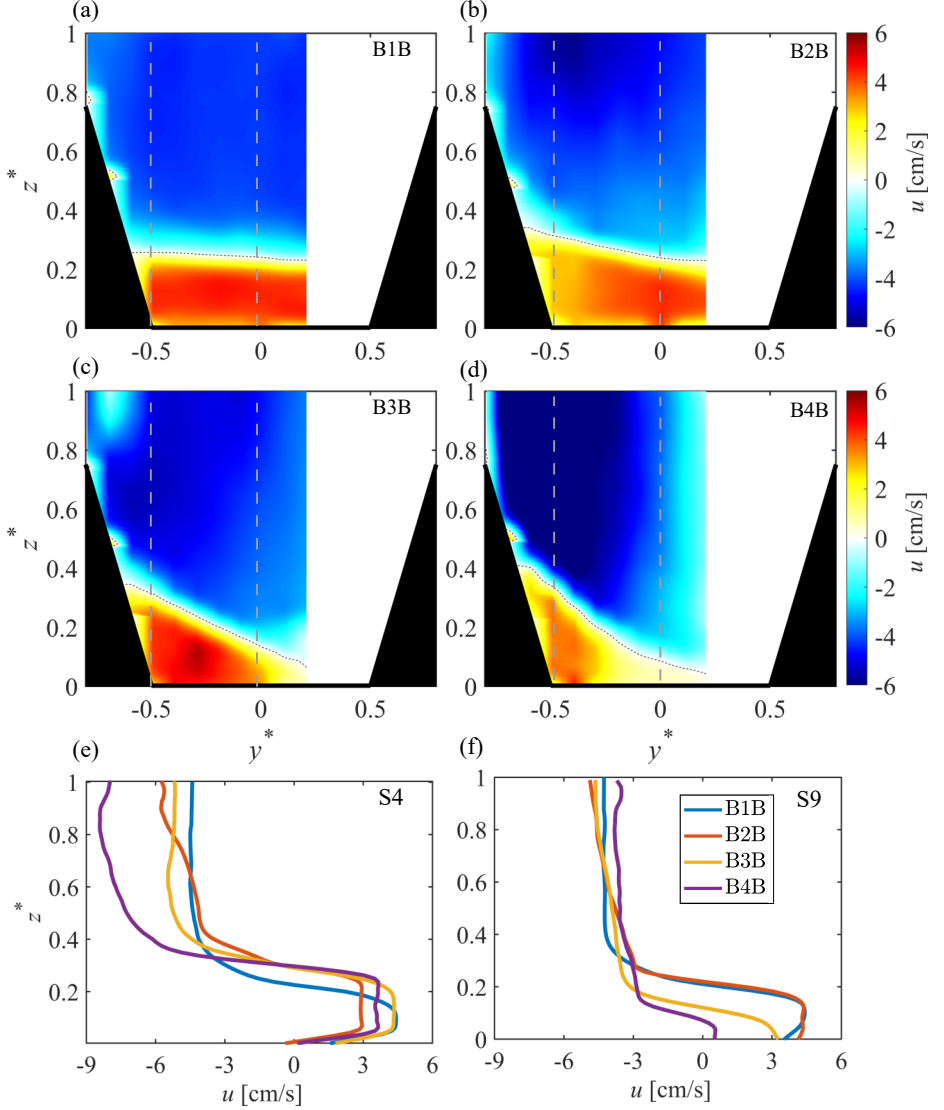
(a)
B1B
(b)
B2B
(c)
B3B
(d)
B4B
(e)
S4
(f)
S9
B1B
B2B
B3B
B4B
z^*
y^*
u [cm/s]

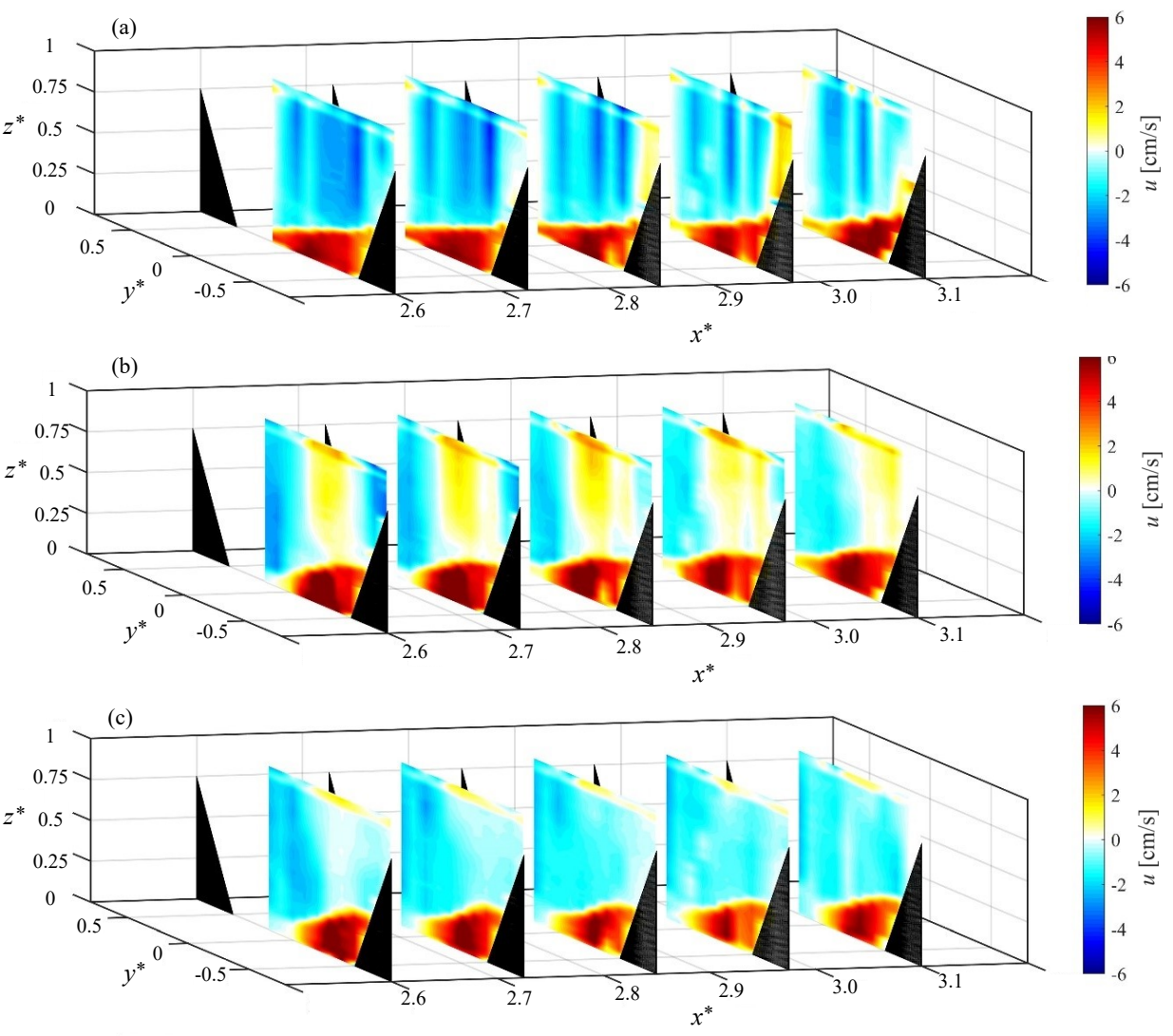
(a)
(b)
(c)
z^*
y^*
x^*
1
0.75
0.5
0.25
0
0.5
0
-0.5
2.6
2.7
2.8
2.9
3.0
3.1
6
4
2
0
-2
-4
-6
u [cm/s]

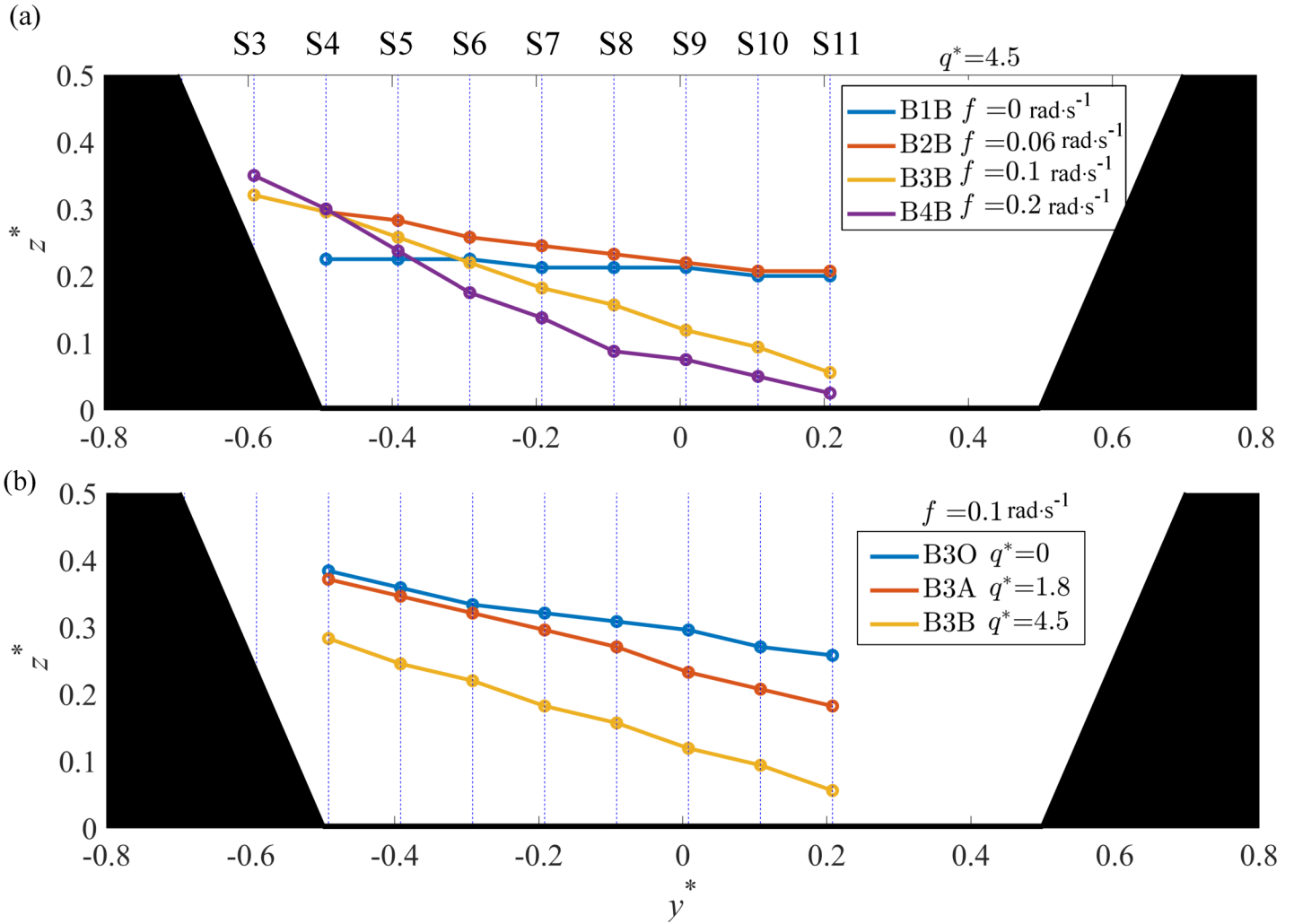
(a)
S3
S4
S5
S6
S7
S8
S9
S10
S11
q^*=4.5
B1B f =0 rad·s^{-1}
B2B f =0.06 rad·s^{-1}
B3B f =0.1 rad·s^{-1}
B4B f =0.2 rad·s^{-1}
z^*
0.5
0.4
0.3
0.2
0.1
0
-0.8
-0.6
-0.4
-0.2
0
0.2
0.4
0.6
0.8
(b)
f =0.1 rad·s^{-1}
B3O q^*=0
B3A q^*=1.8
B3B q^*=4.5
z^*
y^*

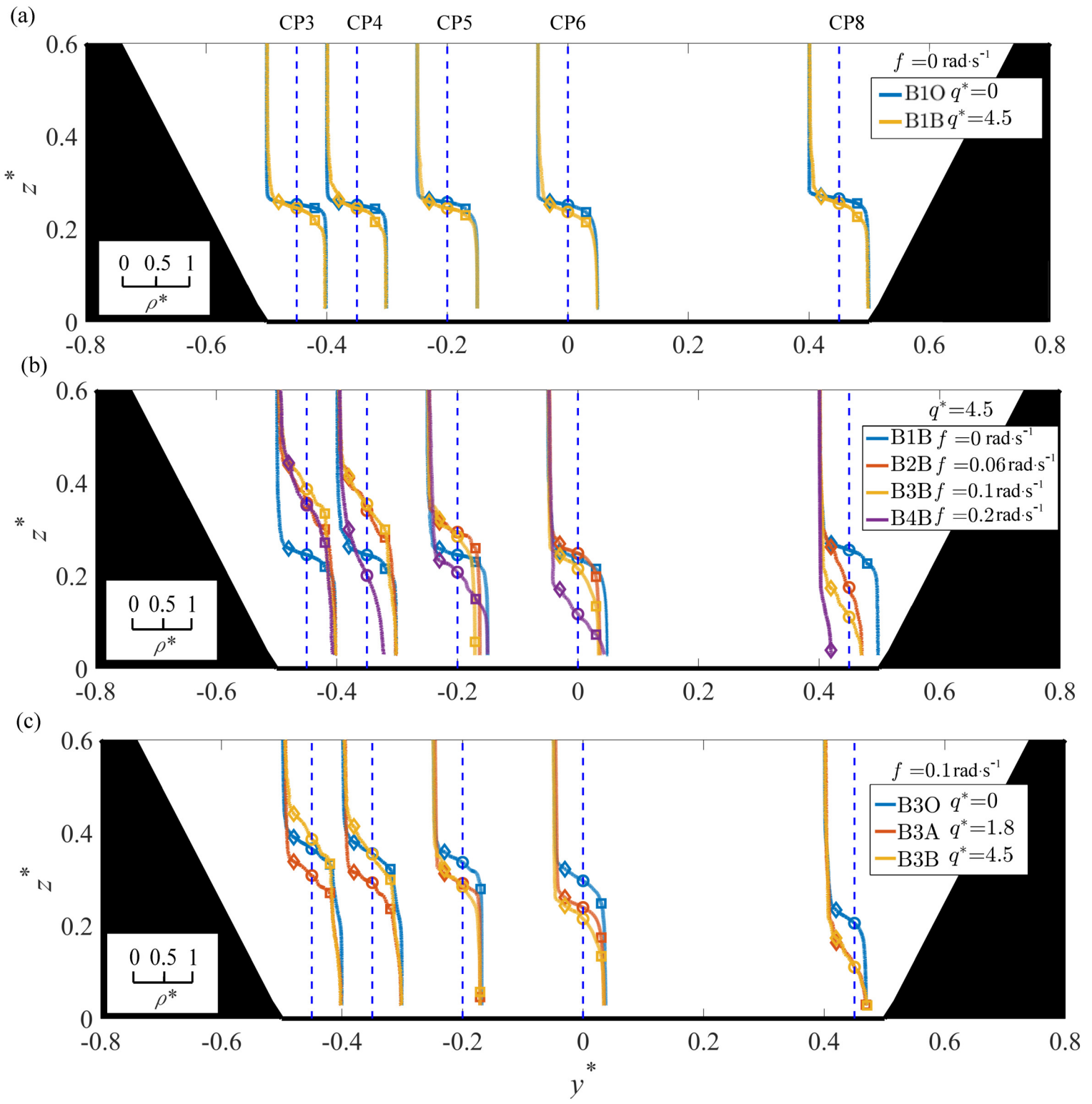
(a)
CP3
CP4
CP5
CP6
CP8
f =0 rad·s^{-1}
B1O q^*=0
B1B q^*=4.5
0 0.5 1
ρ^*
z^*
(b)
q^*=4.5
B1B f =0 rad·s^{-1}
B2B f =0.06 rad·s^{-1}
B3B f =0.1 rad·s^{-1}
B4B f =0.2 rad·s^{-1}
(c)
f =0.1 rad·s^{-1}
B3O q^*=0
B3A q^*=1.8
B3B q^*=4.5
y^*

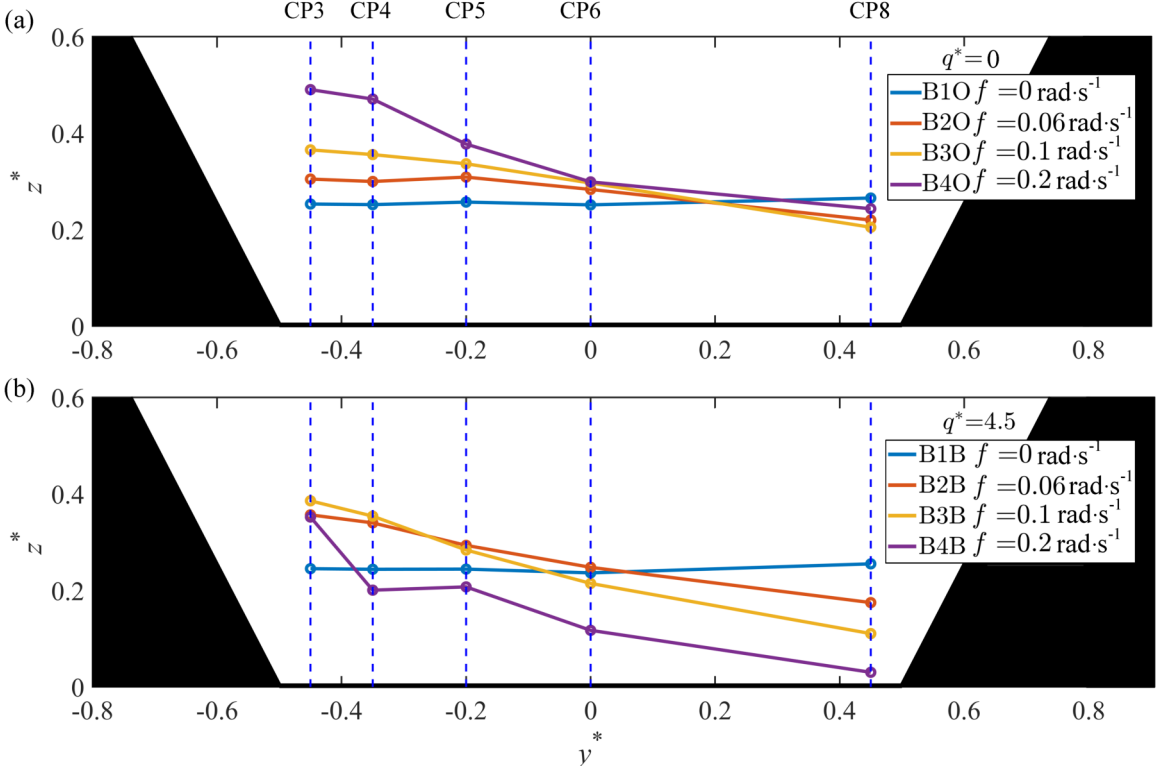
(a)
CP3
CP4
CP5
CP6
CP8
$q^*=0$
B1O f =0 rad·s^{-1}
B2O f =0.06 rad·s^{-1}
B3O f =0.1 rad·s^{-1}
B4O f =0.2 rad·s^{-1}
z^*
0.6
0.4
0.2
0
-0.8
-0.6
-0.4
-0.2
0
0.2
0.4
0.6
0.8
(b)
$q^*=4.5$
B1B f =0 rad·s^{-1}
B2B f =0.06 rad·s^{-1}
B3B f =0.1 rad·s^{-1}
B4B f =0.2 rad·s^{-1}
z^*
y^*

(a)

α_g

$\alpha_{\rho^*=0.5}$

(b)

α_g

α_u

- B1O, f =0 rad · s^{-1}, q^* =0
- B1A, f =0 rad · s^{-1}, q^* =1.8
- B1B, f =0 rad · s^{-1}, q^* =4.5
- B2O, f =0.06 rad · s^{-1}, q^* =0
- B2A, f =0.06 rad · s^{-1}, q^* =1.8
- B2B, f =0.06 rad · s^{-1}, q^* =4.5
- B3O, f =0.1 rad · s^{-1}, q^* =0
- B3A ,f =0.1 rad · s^{-1}, q^* =1.8
- B3B, f =0.1 rad · s^{-1}, q^* =4.5
- B4O, f =0.2 rad · s^{-1}, q^* =0 - Scan 1
- B4O, f =0.2 rad · s^{-1}, q^* =0 - Scan 2
- B4O, f =0.2 rad · s^{-1}, q^* =0 - Scan 3
- B4A, f =0.2 rad · s^{-1}, q^* =1.8 - Scan 1
- B4A, f =0.2 rad · s^{-1}, q^* =1.8 - Scan 2
- B4A, f =0.2 rad · s^{-1}, q^* =1.8 - Scan 3
- B4B, f =0.2 rad · s^{-1}, q^* =4.5 - Scan 1
- B4B, f =0.2 rad · s^{-1}, q^* =4.5 - Scan 2
- B4B, f =0.2 rad · s^{-1}, q^* =4.5 - Scan 3

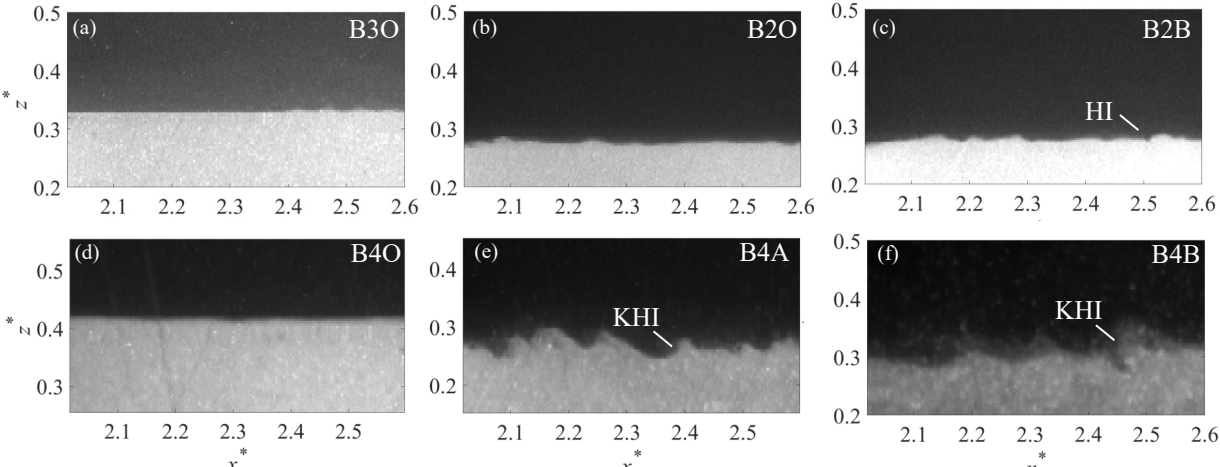
(a)
B3O
(b)
B2O
(c)
B2B
HI
(d)
B4O
(e)
B4A
KHI
(f)
B4B
KHI
z*
x*
0.5
0.4
0.3
0.2
2.1
2.2
2.3
2.4
2.5
2.6

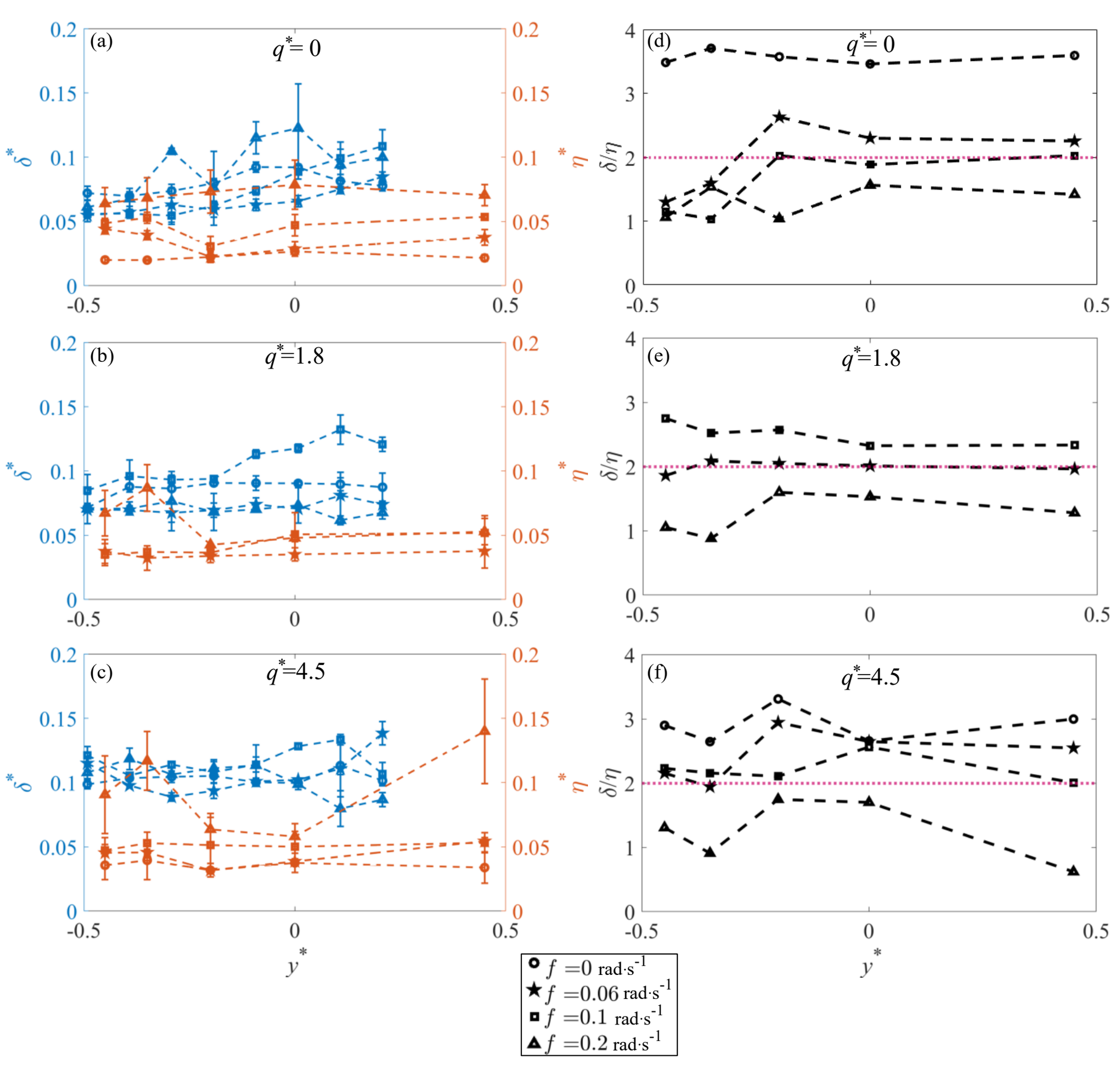
(a)
q^*= 0
(b)
q^*=1.8
(c)
q^*=4.5
(d)
q^*= 0
(e)
q^*=1.8
(f)
q^*=4.5
δ^*
η^*
δ/η
y^*
f =0 rad·s^{-1}
f =0.06 rad·s^{-1}
f =0.1 rad·s^{-1}
f =0.2 rad·s^{-1}

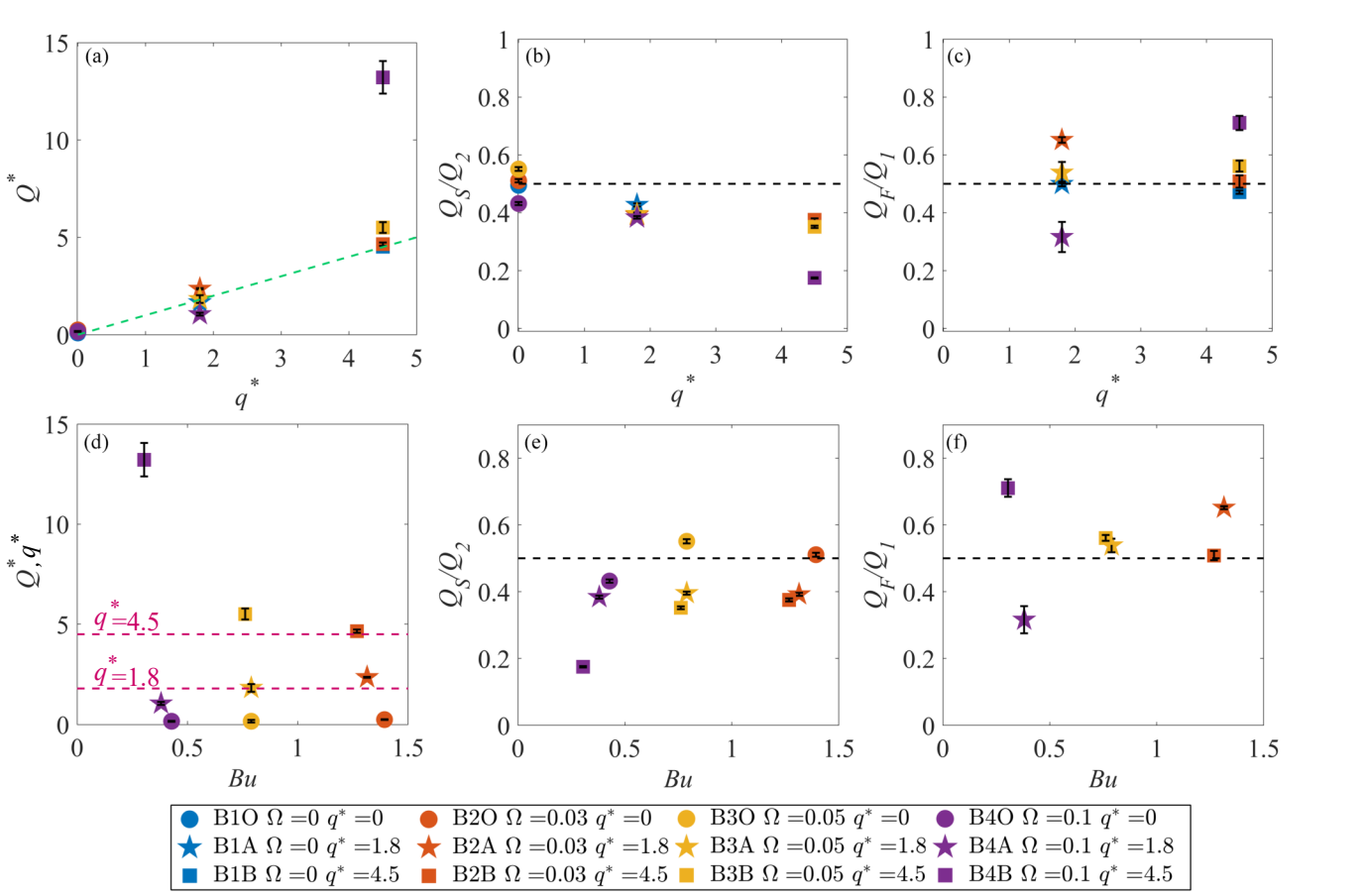
(a)
(b)
(c)
(d)
(e)
(f)
Q^*
q^*
Q_S/Q_2
Q_F/Q_1
Q^*, q^*
Bu
q^*=4.5
q^*=1.8
B1O Ω =0 q^* =0
B1A Ω =0 q^* =1.8
B1B Ω =0 q^* =4.5
B2O Ω =0.03 q^* =0
B2A Ω =0.03 q^* =1.8
B2B Ω =0.03 q^* =4.5
B3O Ω =0.05 q^* =0
B3A Ω =0.05 q^* =1.8
B3B Ω =0.05 q^* =4.5
B4O Ω =0.1 q^* =0
B4A Ω =0.1 q^* =1.8
B4B Ω =0.1 q^* =4.5